High Frequency Quasi-Periodic Oscillations in the X-ray Radiation of the Black Hole Binary GRS 1915+105

by

Jonathan Zachary Gazak

Submitted to the Department of Physics
in partial fulfillment of the requirements for the degree of

Bachelor of Science in Physics

at the

MASSACHUSETTS INSTITUTE OF TECHNOLOGY

June 2006

Author .....
Department of Physics
May 12, 2006

Certified by .....
Ronald A. Remillard
Principal Research Scientist
Thesis Supervisor

Accepted by .....
Professor David E. Pritchard
Senior Thesis Coordinator, Department of Physics

High Frequency Quasi-Periodic Oscillations in the X-ray Radiation of the Black Hole Binary GRS 1915+105

by

Jonathan Zachary Gazak

Submitted to the Department of Physics on May 12, 2006
in partial fulfillment of the requirements for the degree of
Bachelor of Science in Physics

Abstract

GRS 1915+105 is an accreting black-hole in a binary system located in the Milky Way. It is one of the most variable X-ray sources known, and 12 variability classifications have been defined, many of which appear to be repetitive cycles of accretion instability. We study one particular variability type, the ρ cycle, which is selected for its high frequency quasi-periodic oscillations (HFQPOs) and recurring double-peak flare in the light curve. We investigate the primary properties of the 82 ρ-type observations collected by RXTE. The range in flare recurrence time (τ) is 33.73 s $\leq \tau \leq$ 122.49 s, with $<\tau> \pm \sigma_{sample} = 65.44 \pm 19.83$ s. The flaring fraction ζ, defined by percent of cycle exposure $\geq$ 1.2*mean count rate, ranges 12.11% $\leq \zeta \leq$ 37.61%, with $<\zeta> \pm \sigma_{sample} = 20.05 \pm 5.33\%$. We find a correlation between τ and ζ which divides the 82 observations into three sub-classes: ρ_1; slow with low ζ, ρ_2; fast with low ζ, and ρ_3; fast with high ζ. The evolution between sub-classes suggests two driving mechanisms, an unknown mechanism limiting $\tau > 33$ s and a process consistent with the Eddington limit that increases ζ (at the lower limit of τ) for the ρ_3 group. For each subclass we study the emission properties in four phase zones of the ρ cycle, where the phases are defined on the basis of the X-ray count rate (X) and soft color (S; rates at 6-12 keV / 2-5 keV). Two HFQPOs in the ρ cycle are isolated to different zones and sub-classes: one at 67 Hz is localized to the second (hard-spectrum) flare, and another QPO at 150 Hz in the low X, low S phase zone of the ρ_1 group. All phase zones display low-frequency QPOs, and they are particularly strong in the low-X, low-S zone ($\sim$7.5 Hz) and the low-X, high-S zone ($\sim$10.5 Hz). Classifications of X-ray spectral states for each zone indicate no zones in the thermal state, flaring zones (high X) in the steep power law (SPL) state, and quiet zones (low X) in either the hard or hard:SPL intermediate state. We conclude that the ρ cycle provides special opportunities to further study an instability cycle that is driven, in part, by the Eddington limit and that portions of the cycle contain the mechanism that produces two different HFQPOs. Further investigations should be made with increased phase resolution and with additional strategies to define the phases of the ρ cycle.

Thesis Supervisor: Ronald A. Remillard
Title: Principal Research Scientist

Acknowledgments

My first meeting with Dr. Ron Remillard exposed me to his fascinating research on black hole binaries, and I was hooked. The two years of research I conducted under Ron's supervision transformed me from a wide-eyed and, admittedly, clueless student to an undergraduate researcher capable of producing this thesis. Ron has taught me more about the science and art of experimental astrophysics than any undergraduate course work could offer. I thank him for patiently demanding that I learn from my own mistakes, fix my own bugs, and choose the direction of my research. Ron's humorous analogies lightened the countless hours spent polishing this thesis until we finally found ourselves "skiing downhill fast" towards this final document.

Along with Ron, I thank MIT RXTE team members Dr. Al Levine and Dr. Ed Morgan for their availability and willingness to help myself and other students. Al's organization of weekly discussions with scientists and engineers broadened the academic impact of my time as a UROP student, and Ed saved me from many computer troubles and patiently ignored my inability to grasp hard drive usage etiquette.

To all the Professors who have encouraged my interest in physics, I thank you. Of special note, Professor Saul Rappaport's lectures on special relativity first introduced me to astrophysics and Professor Ed Bertschinger's inspired lectures on the inherent beauty of general relativity solidified my interest. Dr. John Makous of Charlotte, NC first introduced me to physics as a serious academic pursuit and played no small part in my decision to attend MIT.

I am forever indebted to my parents, John and Julie Gazak, for allowing (and forcing) me to choose my own path in life, and for supporting my education. I surely could not produce a document like this without their support–and for that I am deeply grateful. Thank you both! My sisters Alexis and Sarah have taught me more about life through friendship and conflict than anyone else, and always help me keep a level head when that life gets rough.

Finally, my girlfriend Lauren Cooney and my friends keep me happy and laughing, even in the whirlwind of MIT. I thank them for their friendship and support.

Contents

List of Figures

List of Tables

Chapter 1

Introduction

1.1 Black Holes and General Relativity

In 1915, Einstein's theory of general relativity (GR) redefined the physics of gravity, creating a theoretical framework matched by data of the period. Among the many consequences of GR is the prediction of exotic compact objects–black holes–where mass dictates implosion to a size within its own event horizon. Debate over the existence of such high gravity objects and the validity of Einstein's physics predicting them lasted decades and entrenched many of the brightest minds of the time. Kip Thorne discusses this battle in his book "Black Holes and Time Warps," an eyewitness account to much of the historical development of present day GR theory and related astrophysics. While few present day astrophysicists doubt the existence of black holes[1], many refused to accept general relativity's prediction of these compact objects prior to the 1960s. Thorne describes two camps of astrophysicists: those such as Chandrasekhar, Zwicky, and Oppenheimer who took Einstein's theory and mathematically predicted stellar conditions where gravity overwhelmed all other known forces. Others, including Eddington, Wheeler, and Einstein himself, argued that

[1] Although an event horizon has not been directly imaged, mounting evidence of numerous black hole candidates more massive than the neutron star limit leave little question of the existence of these objects. [13]

some unknown "law of Nature" must prevent such "absurd" situations.[2]

By the 1960s, most credible astrophysicists accepted that massive stars might collapse, after exhausting their nuclear fuel, into compact neutron stars or even black holes. In a neutron star, gravity compresses the mass of the stellar remnant into into the structure of a single atomic nucleus supported by the strong nuclear force.[3] However, above a critical mass of approximately 3 solar masses ($3M_{\odot}$), gravity overwhelms even the strong nuclear force, causing implosion to physical dimensions within an object's event horizon.[4] At this size, the object ceases to radiate by any conventional means–not even light can escape the object's gravitational pull. No known quantum-mechanical force can withstand the strength of gravity in such a case, and the stellar remnant is thought to collapse into a quantum singularity of unknown dimensions. Yet theory represents only part of the puzzle, and observational verification of compact object existence and behavior remained out of reach. Even as data on neutron stars became available, black holes remained theoretical entities. The problem–and what makes black holes so intriguing: these objects are so massive and compact that within a certain radius called the event horizon, not even light can escape the object's gravity. For this reason, black holes do not radiate at observable levels and cannot be directly imaged by conventional methods of collecting light. Yet the extreme gravity thought to warp spacetime around the object would create curved spacetime environments outside of the event horizon, and strong gravity might cause observable effects on radiating matter that is falling into a black hole. Studying those regions has become a major endeavor of astrophysics. But studying and understanding the physical processes around black holes also requires finding some of them.

[2]Excerpt from Eddington's speech against Chandrasekhar's talk at the 1935 Royal Astronomical Society Meeting. Thorne, K.S., "Black Holes and Time Warps." p. 160.[13].

[3]Thorne, K.S., "Black Holes and Time Warps.' '[13]

[4]Remillard, R.A. and McClintock, J.E. "X-Ray Properties of Black-Hole Binaries" 2006. p. 50.[11].

1.2 Finding Black Holes

A black hole isolated in a region of empty space is nearly impossible to detect, and even detection by a chance occultation would leave little hope of any in depth study of the object. Detecting black holes requires accretion, the infall of matter into a black hole's event horizon. As matter falls into a black hole, it heats dramatically, giving off X-rays. Astronomers find black holes by finding this X-ray emission from accretion systems and then using the binary motions of the companion to show that the compact object has a mass that exceeds the limit for neutron stars. Such systems, where a black hole is being fed significant amounts of material, fall into two basic categories. The first, which is not studied in this thesis, are active galactic nuclei (AGN). AGN lie at the centers of quasars and radio galaxies, galaxy scale objects exercising tremendous energy outflows. In such systems, black holes of millions or billions of times the mass of the sun are active. In quasars, large, hot accretion disks emit energy rivaling any other process in the observable universe. And with the radio galaxy type of AGN, accreting material is fed into enormous radio jets which travel into intergalactic space.[5]

Current observational evidence and theory concerning the development and evolution of galaxies suggests that many–if not all–galaxies surround a central, supermassive black hole millions of times the mass of our sun. While the method by which such supermassive black holes form remains a mystery, observation of active galactic nuclei (AGN) suggests that during galaxy formation, enormous amounts of materials fall into the central black hole, increasing its mass and radiating immense amounts of energy across the electromagnetic spectrum.

The black holes detectible by X-ray radiation investigated in this thesis are stellar black holes, i.e. 3-15$M_{\odot}$ black holes that reside in the Milky Way. Stellar black holes are formed as the final stage in the evolution of massive stars, and have been linked to gamma ray bursts, the brightest known explosions in the observable universe. Stellar black holes which are detectible by astronomers on Earth must be fed by an

[5]Thorne, Black Holes and Time Warps, p. 350-355.[13].

accretion disk. Thus, detectable stellar black holes are locked in close orbits with a stellar companion. These stellar sized black holes in binary systems are termed black hole binaries (BHBs), and high time and spectral resolution studies on these objects resulted in the discovery of previously unknown accretion disk properties. In the Milky Way, the total population of stellar-mass black holes is thought to be ~300 million, but to date, 20 binary systems are confirmed BHBs, meaning the compact object's mass is determined to be greater than $3M_{\odot}$, and thus cannot be a neutron star.[6]

1.3 Black Hole Binary Accretion Disk

As discussed in Section 1.2, all known stellar-size black holes are detected as X-ray sources where an accreting compact object is found to be too massive to exist as a neutron star. Because accretion disks supply the radiation, understanding accretion physics becomes a necessary step towards interpreting the X-ray observations in full detail and learning more about black holes.

1.3.1 The Accretion Process

Accretion is the condition of mass flow between a stellar companion and the compact object. If the binary separation is small enough, the deep gravity potential well of the compact object will allow for a slow process of accretion in which outer gas of the companion star falls onto the compact object. Conservation of angular momentum forbids this gas from falling radially onto a compact object in a binary system, instead dictating an inward spiral and a mechanism to draw angular momentum from the infalling gas.[7]

Infalling matter builds up into an accretion disk surrounding the compact object. As the density of the disk builds, viscosity begins to transfer angular momentum

[6]Remillard, R.A. and McClintock, J.E. "X-Ray Properties of Black-Hole Binaries" 2006. p. 50.[11].

[7]Such inward spiral is expected to begin with Keplerian orbits, but in the inner accretion disk material must follow orbital paths described by the Kerr Metric of a spinning spherical mass.

outward and matter spirals onto the surface of a neutron star, or into the event horizon of a black hole. The exact prescription of viscosity is unknown, but a leading theory suggests that viscosity scales with pressure, thus increasing with temperature. The material is further heated as it falls closer to the black hole, deep within it's gravitational well.[8] The gravitational energy heats the disk material, which reaches roughly ten million degrees, emitting X-rays. This model does not account for all of the observed properties of accretion, e.g., relativistic jets are observed in many black hole binary systems with on/off cycles that are not understood. Such phenomenon require more extensive theoretical framework; taking into account electromagnetic activity as a result of a turbulent plasma spiraling into a spinning (Kerr) black hole. Such theories may explain how material from the inner disk is ejected anisotropically and in well collimated beams–jets.[9]

Because these X-rays pass through the gas and dust in the plane of the Milky Way, they represent a far reaching window in which to study accretion disks surrounding compact objects anywhere in the Milky Way. X-rays also offer the advantage of being emitted extremely close to the event horizon–up to the innermost stable circular orbit (ISCO) that represents the final limit of the accretion disk, according to general relativity.

1.3.2 Accretion Disk Spectra

The simplest models of accretion disks predict that energy that is made available as matter moves in successively smaller orbits in the disk is released locally as thermal, black body emission. Evidence of such a disk black body is seen in the spectra of BHBs, yet this thermal disk is often accompanied or completely dominated by emission of a different distinctly nonthermal type, modeled by a power law. The physical system responsible for such nonthermal spectral emission is poorly understood. A brief explanation of the four principal spectral states of BHBs is given here

[8] "McClintock, J.E., and Remillard, R.A., "Black Hole Binaries." 2003. p. 9.[12].

[8] "McClintock, J.E., and Remillard, R.A., "Black Hole Binaries." 2003. p. 9.[12].

[9] "Blandford, R. D. "To the Lighthouse." 2002. p. 12-20 Published in "Lighthouses of the Universe."[2].

and these states are revisited in Chapter 5, where the spectral research for this thesis is discussed.

While accretion disks often emit blackbody spectra, recent observational studies of the spectra and intensity of such X-ray emission have exposed a variety of spectral states far more complex than current theory describes. The problem: physical processes governing conditions such as the power law spectrum and transient radio jets are poorly understood. A robust model for all forms of accretion physics is a major target of present astrophysics. Such a theoretical framework will include observational tests of general relativity in the strong field limit where the revolutionary ideas of Einstein's theory manifest most readily. The work presented in this paper contributes original observational research that is relevant to this effort.

Four main spectral states are observed in black hole binaries. The simple model of a thermal accretion disk is the paradigm for the "thermal" state, where most of the energy flux is due to thermal emission from a multi-temperature accretion disk. The typical temperature of the inner disk is $\sim$1 keV.[10]

The next state, the "hard" state, displays a hard power-law component dominating the spectrum at 2-10 keV. This power law is well modeled with a photon index $\Gamma \approx 1.7$ where the spectrum $N(E) \propto E^{-\Gamma}$. In the hard state the accretion disk appears large and cool at it's inner radius, and the thermal flux decreases significantly or disappears. This X-ray spectrum is associated with the presence of a radio jet, but the physical system dictating such emission has not been modeled with great success.[11]

The third spectral state exhibits both thermal and power law components contributing significant flux, resulting in a mixed spectra and often intense X-ray luminosity. This state is deemed the "steep power law" (SPL) state. Here, a power law component is seen and it is significantly steeper ($\Gamma \approx 2.5$) than in the hard state.[12] The SPL state in BHBs generally exhibits X-ray quasi-periodic oscillations in the range 0.1 to 20 Hz.

Finally, Most BHB systems are X-ray transients that spend time (and generally

[10] "McClintock, J.E., and Remillard, R.A., "Black Hole Binaries." 2003. p. 23.[12].
[11] "McClintock, J.E., and Remillard, R.A., "Black Hole Binaries." 2003. p. 24.[12].
[12] "McClintock, J.E., and Remillard, R.A., "Black Hole Binaries." 2003. p. 25.[12].

a large percentage of their lifetimes) in a quiescent state, where emission from the accretion disk is minimal but nonzero. Emission in this quiescent state is "extraordinarily faint . . . with a spectrum that is distinctively nonthermal and hard."[13] This power-law emission is fit with photon indices from 1.5 to 2.1, and the quiescent state may be related to the hard state.

1.4 Studying Black Hole Binaries

The first satellites capable of studying X-ray emission of compact object binaries provided "a broad understanding of the emitting systems,"[14] justifying the development of future missions to study specific unanswered questions. One second generation mission, the Rossi X-ray Timing Explorer satellite (RXTE), was launched in December 1995 to study, with microsecond time resolution, X-ray intensity variations and spectra of various sources including accreting compact objects in binary systems. The high temporal resolution and wide spectral capabilities (2-200 keV–greater than any previous individual mission) of RXTE provides a single platform capable of studying a wide range of targets with an aggressive response to X-ray transients.

The RXTE satellite contains three instruments for the study of X-ray transients. First, the All Sky Monitor (ASM) is comprised of three Scanning Shadow Cameras (SSC) which use a coded mask and imaging proportional counter to monitor large areas of the sky. While each SSC can refine a source's location to an area of 3' x 7°, the crossed positions of two SSC detections can localize a weak source to within 0.2°, and a strong ($\approx 5\sigma$) source to 3'.[15] This instrument allows for the monitoring of active transients and rapid discovery of new ones, so that targeted data collection may begin as soon as possible after eruption from quiescence. With a sensitivity bandwidth of 2-10 keV, the ASM is sensitive to the bulk of BHB emission, and is used to make detections and monitor general transient activity.

The Proportional Counter Array (PCA) and the High Energy X-ray Timing Ex-

[13] "McClintock, J.E., and Remillard, R.A., "Black Hole Binaries." 2003. p. 25.[12].
[14] Bradt, H. et all, "X-ray Timing Explorer: Taking the Pulse of the Universe." p. 6.[3].
[15] Bradt, H. et all, "X-ray Timing Explorer: Taking the Pulse of the Universe." p. 17.[3].

periment (HEXTE) are used for pointed observations of specific sources of interest. The PCA consists of five large-area proportional counters with the ability to discriminate pulse-heights (which is $\propto$ X-ray energy) into 255 bins, with 20% intrinsic spectral resolution and overall sensitivity between 2-60 keV.[16] In addition to spectral sensitivity, individual PCA proportional counter units (PCU) can be used for extremely high time resolution, capable of timing photon arrivals to within $\sim 1\mu$s. Having 5 PCUs offers the advantage of collecting both broadband spectra and high timing resolution with large collecting area.[17] The HEXTE instrument is aligned to view the same location as the PCA, and contains two groupings of four NaI/CsI detectors sensitive from 20-200 keV While at least one cluster of detectors is always aimed at the source, the units are rocked back and forth, allowing the detectors to collect data on the source and simultaneously very sensitive background readings, allowing for high quality high energy spectra.[18]

The data used for this investigation is largely PCA data and almost entirely (with the exception of occasional references to radio jet results) RXTE data.

1.5 High Frequency Quasi-Periodic Oscillations

The RXTE mission discovered several types of X-ray oscillations that are found at high frequencies, i.e. $\nu > 50$ Hz. One class of these is high-frequency quasi-periodic oscillations (HFQPOs) of hundreds of cycles per second. While low frequency QPOs (0.01 - 50 Hz) are common in X-ray compact object binaries, they are beyond the scope of this investigation and will not be discussed in any detail. HFQPOs suggest that accretion favor dynamical frequencies, which are possibly associated with particular orbital frequencies. Observationally, HFQPOs are transient in a given X-ray source and the frequencies depend on the spectral state and the individual system.

While the exact nature and cause of HFQPOs in BHB systems is currently unknown, developing a basic understanding of more general quasi-periodic processes

[16]Bradt, H. et all, "X-ray Timing Explorer: Taking the Pulse of the Universe." p. 12.[3].
[17]Bradt, H. et all, "X-ray Timing Explorer: Taking the Pulse of the Universe." p. 14.[3].
[18]Bradt, H. et all, "X-ray Timing Explorer: Taking the Pulse of the Universe." p. 16.[3].

observable in nature may provide insight into the workings of compact object HFQPOs. QPOs are by no means a new phenomenon–the timing between drips from a leaky faucet is a quasi-periodic oscillation–but astrophysical QPOs differ from systems explainable by classical physics in a number of ways.

First, the highest frequency HFQPOs (up to 450 cycles per second), provide evidence for structure in the very inner accretion disk and offer the chance to study these environments of extreme gravity. The most extreme HFQPOs are as fast as the orbits of the very inner accretion disk, or innermost stable circular orbit (ISCO), beyond which no circular orbit is physically possible. Exploring this part of the disk gives astronomers a look at material in the strongest gravity we can hope to study, near the limit where not even X-rays emitted by the material can escape. These high frequencies make understanding the physical system which excites such QPOs in the accretion disks of compact object binary systems particularly important to the goal of investigating GR in the strongest gravitational fields. In addition, because the event horizon of a black hole has never been directly imaged, and because as a black hole's spin increases the event horizon and ISCO draw closer together, HFQPOs may someday add to the mounting evidence of the existence of black holes.

Second, recent research has shown that when a BHB system is capable of exciting a pair of HFQPOs, the frequencies are locked in a 3:2 ratio. This ratio suggests that HFQPOs may be a resonance phenomenon of GR. This interpretation is different from Fourier harmonics that might appear in a 1:2:3 ratio for non-sinusoidal signals. The HFQPO frequency pairs in BHBs are not seen as Fourier harmonics for two reasons. First, the HFQPOs locked in 3:2 frequency ratios are not usually excited at the same time. Second, they lack of a fundamental frequency, i.e. only the $2\nu_o$ and/or $3\nu_o$ appear.[19]

Finally, there is an important difference that separates the HFQPOs of BHB systems to HFQPOs in neutron star binaries. HFQPOs in BHB systems do not change frequency within limits of $\pm 15\%$, despite large changes in luminosity, while neutron star HFQPOs can vary in frequency by factors of more than two. For this reason,

[19] "McClintock, J.E., and Remillard, R.A., "Black Hole Binaries." 2003. p. 45-48.[12].

individual BHB systems excite QPOs of set frequencies, leading researchers to believe that high frequency QPOs in BHB systems are "a stable signature of the accreting black hole."[20] While each BHB system known excites different characteristic QPO frequencies, the spectral properties present during HFQPO excitation appear to be similar for all BHBs. Additional research shows that the frequency of BHB HFQPOs may be dependent on the mass ($\propto M^{-1}$),[21] which is telling of a general relativistic effect.

1.6 Goals of this Thesis

The work in this paper studies data from one black hole binary system collected by RXTE, GRS 1915+105, in hopes of aiding in the global effort to understand QPOs and eventually develop an accretion disk theoretical framework capable of testing general relativity. In such an effort, certain basic questions arise. What excites such high frequency QPOs? What determines a source's characteristic QPO frequencies? How do spectral changes relate to QPO excitation and QPO frequency?

Active black hole binary systems radiate in three main spectral states, one which can be well modeled by a thermal disk blackbody, and two types of power law spectra. Many of the HFQPOs in observed systems occur while the system radiates a steep power law spectrum, but because the physical system capable of producing such spectra is poorly understood, the method of exposing processes responsible for QPO excitation in this paper will focus on a 67 Hz QPO of GRS 1915+105, the one HFQPO that sometimes appears in a thermal state.

GRS 1915+105 is a unique BHB that has been classified to have 12 types of light curves, many of which are obviously representative of instability cycles. One particular cycle is studied in this paper. Over 320000 seconds of data have been collected in 82 observations of the "ρ-type" light curves[22] which accounts for 8% of

[20]Remillard, R. A. "X-ray Spectral States and High-Frequency QPOs in Black Hole Binaries." 2005. p. 3.[10].

[21]Remillard, R. A. "X-ray Spectral States and High-Frequency QPOs in Black Hole Binaries." 2005. p. 3.[10].

[22]T. Belloni, et al. "A model-independent analysis of the variability of GRS 1915+105."[1]

all data collected on the source by RXTE.

The ρ-type observations are highly variable and consist of a periodic cycle of high count rate flares with two peaks of different X-ray color, followed by a more quiet period of low count rate. Averaging all data collected while GRS 1915+105 radiated in the ρ class exposes a 67 Hz QPO of 3.50σ which links this QPO to the cycle and rases the question as to whether a particular section of the ρ variability cycle might excite a far more significant 67 Hz QPO. A method of phase-separating the variability cycle is described and applied to study the fast spectral changes between different phase intervals. The method offers promise as a standard tool for application to additional variability cycles of GRS 1915+105 and similar cycles that are rarely seen in other sources.

The ρ cycles were studied in a general manner, leading to the separation of the 82 ρ observations into three sub-classes. The sub-classes exhibit some differences in observational properties, including a difference in the ability to excite the 67 Hz QPO.

Chapter 2

Black Hole Binary GRS 1915+105

2.1 The GRS1915+105 System

Astronomers have observed 20 confirmed black hole binary (BHB) systems, of which three are classified as persistent sources and 17 as transient X-ray novae.[1] These X-ray transients are marked by intense periods of X-ray activity followed by extended periods of quiescence in which radiation from the accretion disk is minimal. While many X-ray novae–both BHB and neutron star binary systems–have been observed in an active state only once, the systems are believed to be cyclic with recurrence periods which may be many decades to hundreds of years or longer.[2]

Current thought attributes the cycle of outburst and quiescence to a "disk instability mechanism," governed by the density of a system's accretion disk. When a disk is thin, material remains in stable Keplerian orbits around the central black hole. As material continues to accrete from a companion into the disk, the surface density increases to a point when, as discussed in section 1.3.1, viscosity begins to transfer angular momentum outward and material spirals inwards towards the black hole.

The BHB of interest in this paper, GRS1915+105, represents one of the 17 transient sources. GRS1915+105 erupted from quiescence in August of 1992 and has

[1]Remillard, R.A. and McClintock, J.E. "X-Ray Properties of Black-Hole Binaries" 2006. p. 51.[11].

[2]Remillard, R.A. and McClintock, J.E. "X-Ray Properties of Black-Hole Binaries" 2006. p. 51.[11].

remained bright for over thirteen years. Among transients, the duration of intense X-ray radiation from GRS1915+105 is uniquely long; far longer than limits of current theoretical models for the disk instability mechanism for X-ray transients.

GRS 1915+105 was first detected on August 15th, 1992 by the WATCH all-sky monitor (sensitive to 6-150 keV) on the Russian X-ray satellite Granat. Soon after, the Very Large Array (VLA; 27 25-meter radio telescopes located in New Mexico) detected variable radio emission from the same source. This radio data was determined to be jets of apparent superluminal velocities, aiding in the determination of GRS 1915+105 as a BHB system as superluminal jets had only been previously seen in active galactic nuclei (AGN–galactic central engines thought to be supermassive black holes).[3] While jet material does not travel faster than the speed of light ($\frac{v_{jet}}{c} < 1$), the material is ejected at very high speeds and the geometry of the system relative to observers on Earth gives an apparent $\frac{v_{jet}}{c}$ of greater than 1. The production of jets at apparent superluminal velocities classifies GRS 1915+105 as a "microquasar."[4]

GRS1915+105 lies within the Milky Way, (12.5 $\pm$ 1.5) kiloparsecs from earth.[5] The primary compact object has a mass of approximately (14 $\pm$ 4) $M_{\odot}$,[6] as determined by the mass function which requires knowledge of the system's orbital period or the mass of the secondary star.[7] The orbital period, P_{orb}, of GRS1915+105 is 33.5 days with a separation between the compact primary and stellar secondary of a $\approx$ 95 AU. The size of the GRS 1915+105 system is notably large. For comparison, the mean distance between Pluto and the Sun is only 40 AU. In GRS 1915+105, the companion is a red supergiant, as inferred from the large binary separation, and the infrared absorbtion lines in the companion star's spectrum. The size of the GRS 1915+105 system is greater than any other known binary.[8] These quantities are diffi-

[3]Greiner, J., Morgan, E. H., and Remillard, R. A. "RXTE spectroscopy of GRS 1915+105." 1998.[6]

[4]Remillard, R., Muno, M., McClintock, J., and Orosz, J. "X-ray QPOs in Black-Hole Binary Systems." 2002. p. 4.[8].

[5]Morgan, Remillard, and Greiner. "RXTE Observations of QPOs in the Black Hole Candidate GRS 1915+105." 1997. p. 1.[7].

[6]Greiner, Cuby, and McCaughrean. "An Unusually Massive Stellar Black Hole in the Galaxy." Nature, 414, 522. 2001.[4].

[7]McClintock, J.E., and Remillard, R.A., "Black Hole Binaries." 2003. p. 3.[12].

[8]Remillard, R.A., and McClintock, J.E., "X-Ray Properties of Black-Hole Binaries" 2006. p.

cult to determine precisely: the source lies behind the Milky Way's Sagittarius arm, limiting optical observation of the secondary stellar component.[9] In addition, observation of a BHB secondary star is generally limited to periods of quiescence when and X-ray emission from the accretion disk drops to minimal levels. The accretion disk of GRS1915+105 does enter periods of low, steady X-ray emission, but has yet to enter full quiescence.

2.2 X-Ray Light Curves of GRS 1915+105

The black hole binary (BHB) GRS1915+105 has been a steady target of the RXTE satellite since the program launch in late 1995. Early observations showed that the source went through periods of steady activity and periods of variability greater than any other observed X-ray binary novae in history.[10]

The design of RXTE allows astronomers to take observations of GRS 1915+105 in a number of different high-speed data collection modes, but all observations are capable of producing light curves binned to one second. These observations range in length from 465 to 27094 seconds with an average exposure time of around 5500 seconds.

Light curve types are, in a very general way, separable into "steady" and "variable" classes, determined by the variance in the total count rate of the light curve over time. One measure of variability, for example, is $\frac{\sqrt{<counts^2>-<counts>^2}}{<counts>}$, or σ/μ, where σ is the sample standard deviation and μ is the mean count rate. The count rate and source variance are sufficiently high in this source that the measured value of σ is always far greater than the standard deviation due to counting statistics (σ_{stat}), so that $\sigma \approx \sigma_{source}$.

Three very different types of observations are shown in Figure 2-2. While "steady"

51.[11].

[9]Greiner, Morgan, and Remillard. "Rossi X-ray Timing Explorer Observations of GRS 1915+105." 1996. p. 1.[5].

[8]Greiner, Morgan, and Remillard. "Rossi X-ray Timing Explorer Observations of GRS 1915+105." 1996. p. 1.[5].

[10]T. Belloni, et al. "A model-independent analysis of the variability of GRS 1915+105."[1]

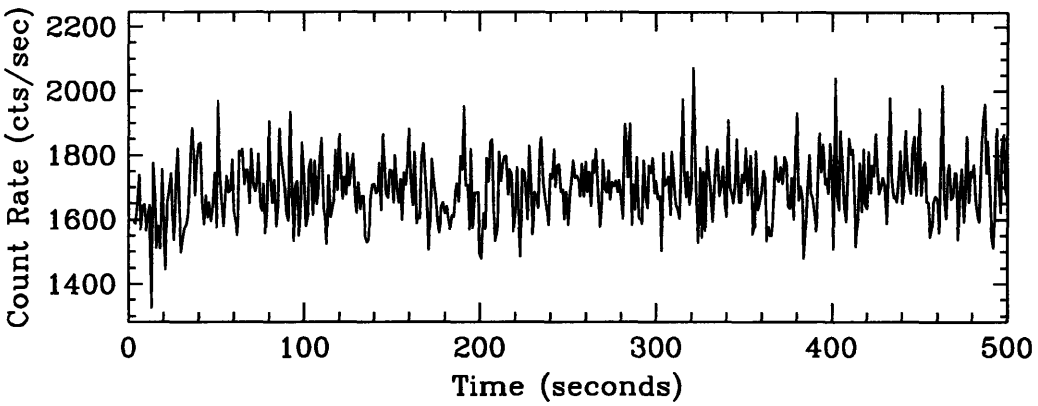

Figure 2-1: A 500 second X-ray light curve of GRS 1915+105 (2-50 keV) for the observation of XTE day 0948. This is a steady state observation, classified as type chi χ, by Belloni et al. (2001), indicating roughly steady mean count rate with a hard spectrum.

and "variable" classifications allow for an important distinction between X-ray emission modes of GRS 1915+105, the different manifestations of a high variability (σ/μ) observation apparent in Figure 2-2 expose the need for a more refined separation between different modes of emission, or different "observation types."

The three light curves in Figure 2-2 represent only a few of many variable observation types of GRS 1915+105. Yet even with the great differences shown in Figure 2-2, early observations of GRS 1915+105 showed that the source's behavior was confined to a finite set of light curves, many of which show variability patterns that are clearly distinct and repetitive. As documented in the next subsection, GRS 1915+105 was found to oscillate between a small set of radiating conditions, as a type of building block for the types of light curves. Astronomers realized rapidly that a classification system for these observations was needed. Such a classification system of GRS 1915+105 observations would enable further study on any one "type" of observation by combining the exposure times of groups of similar observations of to take advantage of better data analysis statistics.

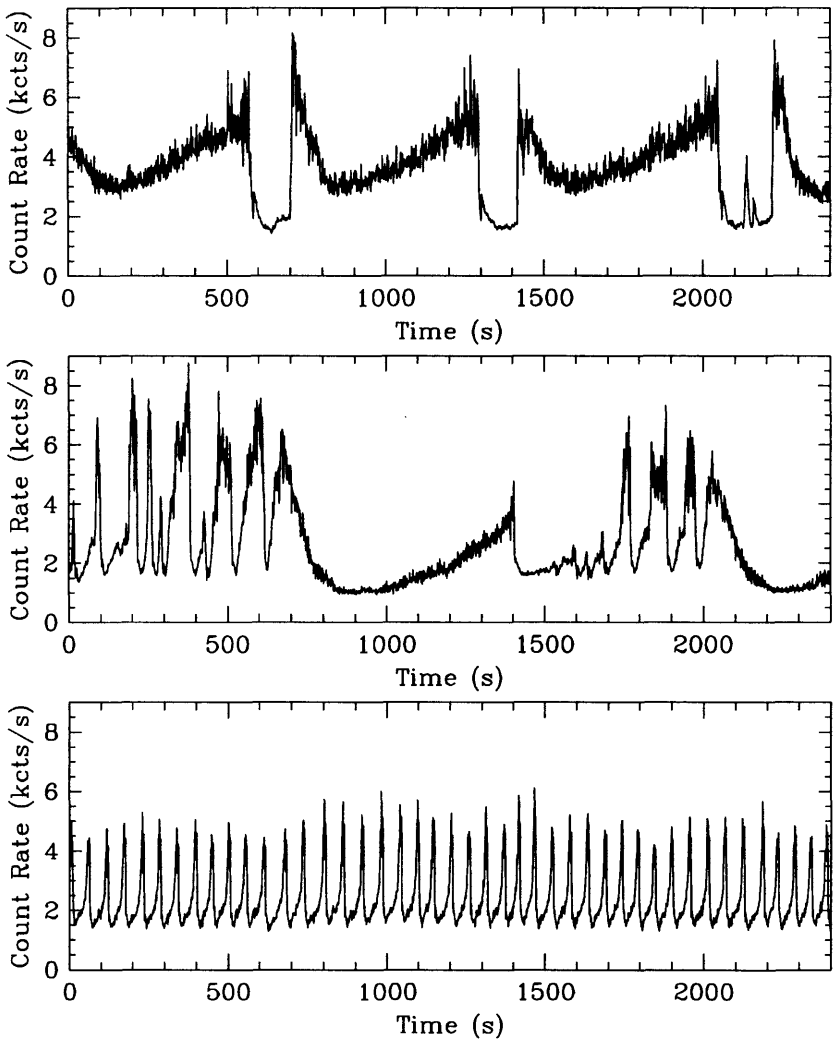

Figure 2-2: Three 2400 second light curves (2-50 keV) illustrating variable types of observations: type θ (top; day 1354a), type β (middle; day 4352a), and type ρ (bottom; day 1268).

2.3 Variability Types of GRS 1015+105

In late 1999, enough data had been collected to allow a team studying the complex and often variable RXTE observations of GRS 1915+105 to divide 163 observations into 12 classes by studying both count rate and color properties.[11]

While the very form of GRS 1915+105's X-ray light curves (as in Figure 2-2) indicated a need for a classification system, the system was developed with significant

[11]T. Belloni, et al. "A model-independent analysis of the variability of GRS 1915+105."[1]

consideration of rough spectral properties as well. By collecting data in three coarse energy bands, A, B, and C (2-5, 5-13, and 13-50 keV, respectively) spectral shapes may be generically examined in terms of a ratio of count rates in two energy bands. Such ratios are known as an X-ray "color."

In Figure 2-3, two of the three plots from Figure 2-2 have been re-plotted with two additions. A plot of Hard Color (C/B or 13-50/5-13 keV) vs. count rate is defined as a "color-intensity" diagram, and a plot of Hard Color vs. Soft Color (B/A or 5-13/2-5 keV) is a "color-color" diagram. Both diagrams were used in the initial classification system, and their patterns convinced Thomas Belloni and his team that the highly variable modes of GRS 1915+105 might represent only three quasi-stable emission modes through which the system oscillated, with different sequences and time scales, manifesting as 12 observation classes.[12]

Just as the light curve of an observation can wash out details of the energy spectra of a source by combining all X-rays of energy between 2 and 50 keV, so do the color-intensity and color-color diagrams mask fine spectral properties, and also the direction of temporal variations. All three plot types are extremely helpful in investigating different observation types, and markers have been found on these diagrams for other properties, such as quasi-periodic oscillations and jets. The RXTE satellite equipment allows for much higher resolution spectral and timing studies, and in general, one second light curves and three channel color plots are simply diagnostic tools for more detailed analyses.

X-ray data analyses also utilize higher resolution data (temporal and spectral) for spectral fitting as well as conducting Fourier analyses to search for temporal signatures over a large range in frequency. Any measurement intervals defined from the light curve, color-intensity, and color-color diagrams can be used to select corresponding data with high temporal resolution or high spectral resolution with a directed interest– to gain physical insights as to how the system behaves.

[12]T. Belloni, et al. "A model-independent analysis of the variability of GRS 1915+105."[1]

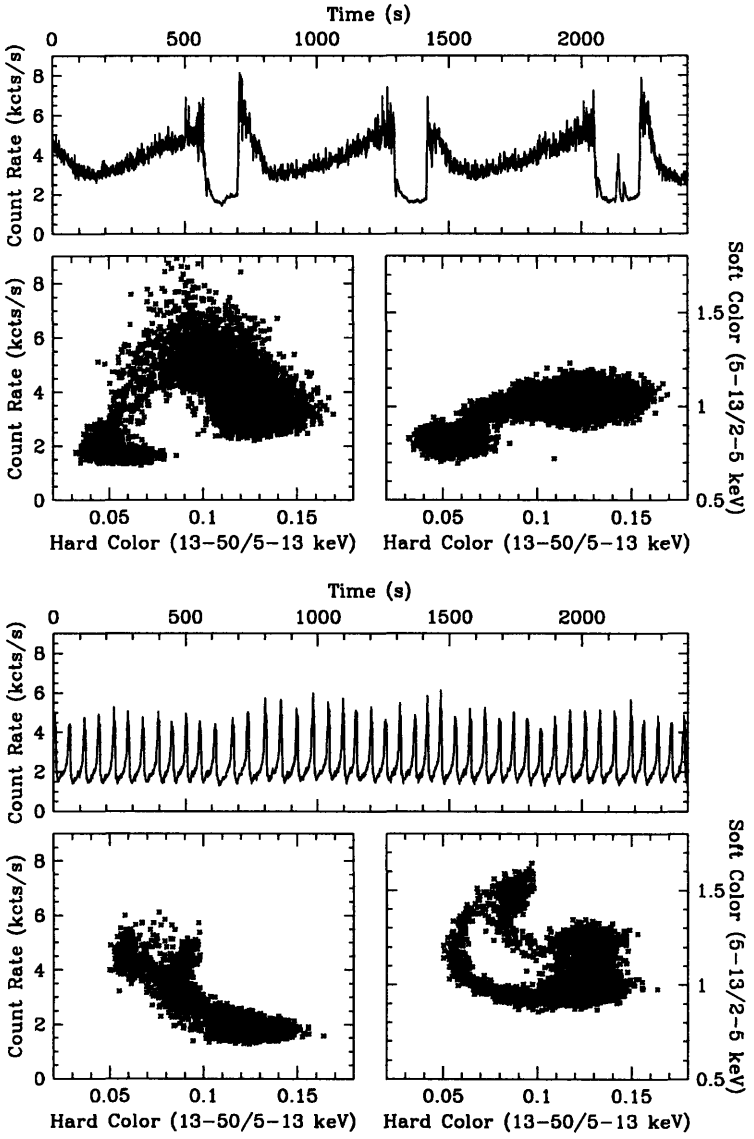

Figure 2-3: The θ-type and ρ-type light curves (see Fig. 2-2) are shown again; along with color-color and color-intensity diagrams that display the same data in these formats.

2.4 Power Density Spectra of GRS 1915+105

In BHBs such as GRS 1915+105, the amount of variability is a function of frequency, and there is particular interest to examine fluctuations at high frequency, i.e. up to the dynamical frequencies near the BH ISCO. The RXTE satellite is capable of microsecond time resolution, and was built for the purpose of studying oscillations

occurring hundreds of times per second. The diagnostic visual studies of light curves such as those in Figure 2-3 are only adequate to recognize and roughly estimate high amplitude and low frequency oscillations. To locate and study oscillations such as HFQPOs, different mathematical tools must be used.

A method of Fourier analysis, the fast-fourier transform, is used to decompose the time stream of X-ray measurements into the frequency domain. The technique calculates amplitudes of variability in each frequency bin. The Fourier power (amplitude squared) can be normalized to express the power of the fluctuations relative to the average flux of the source. This data, which can be plotted as power vs. frequency in a power density spectrum (PDS), provides the frequency resolution to study oscillation timescales at which a source radiates preferentially.

Three PDS of an observation classified as type rho (ρ) are plotted in Figure 2-4. Each PDS in Figure 2-4 represents a fast-fourier transform of a different energy window of a single observation. While the basic form of the three PDS may be similar, and the statistical scatter of the hard energy window (13-50 keV, right in Fig 2-4) at high frequency is due to lower count rates in that window. Significant differences between the three bands can be found and are used to understand a source. While many HFQPOs are found strongest in the sum band (2-30 keV, left in Fig 2-4), some do appear strongest in the medium-hard band (6-30 keV, center in Fig 2-4). For the remainder of this section PDS displayed will be of the medium-hard band. The medium-hard band of all averaged ρ observations is shown in context with four other light curve types in Figure 2-5, and the chosen types include those with light curves displayed in Figure 2-2.

The comparison between PDS of different observation types begins with low frequency behavior ($\nu < 1$ Hz). Here, "steady" observation types (χ, γ in Fig. 2-5) clearly show a lack of low frequency structure which manifests visually in light curves (see Fig. 2-1), and mathematically as a low value of σ/μ per frequency bin (discussed in Section 2.2). Highly variable observation types (ρ, β, θ in Fig. 2-5) show more power in the low frequency region. In some cases, as with ρ PDS, the actual quasi-periodic recurrence frequency of flares in the light curve (see Figs. 2-3, 2-2) manifests

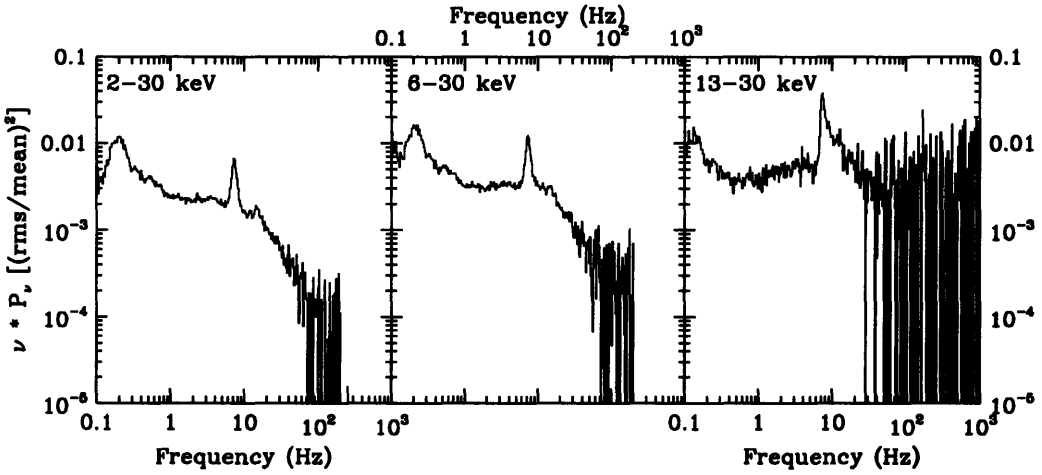

Figure 2-4: Three PDS of the same ρ day (GRS 1915+105 day 2699b) in different energy bins. Sum band, 2-30 keV (left), medium-hard band, 6-30 keV (center), and hard band, 13-30 keV (right).

in an observable fashion as a very low frequency spike in the PDS accompanied by a number of harmonic spikes. These harmonics are mathematical signatures of non-sinusoidal oscillations such as the ρ flares.

In the frequency window from 1-40 Hz, strong low frequency QPOs (LFQPOs) are clear in the ρ example at 10 Hz, χ at 3-4 Hz, and γ at 30-40 Hz. Observations of type θ and β have weaker LFQPOs at 10 and 8 Hz, respectively.

At frequencies greater than 40 Hz, HFQPOs are difficult to separate from the noise in a PDS of a single observation. For this reason, the enormously powerful 67 Hz HFQPO in the γ sample is particularly interesting. Astronomers studying PDS plots of RXTE data first discovered HFQPOs, and cases where these results are as strong as the γ plot in Figure 2-5 helped to motivate this study. In average PDS over many ρ observations a weaker 67 Hz detection appears (marked with an arrow in the top panel of Figure 2-5) and motivates a main question investigated in this thesis. Do small phase sections of variable sources exhibiting weak HFQPOs provide all of the power for the HFQPO, i.e. is the strength of the γ 67 Hz HFQPO present in variable observation types as well, where large amounts of non-QPO data weight down the results in plots which investigate the entire variability phase cycle?

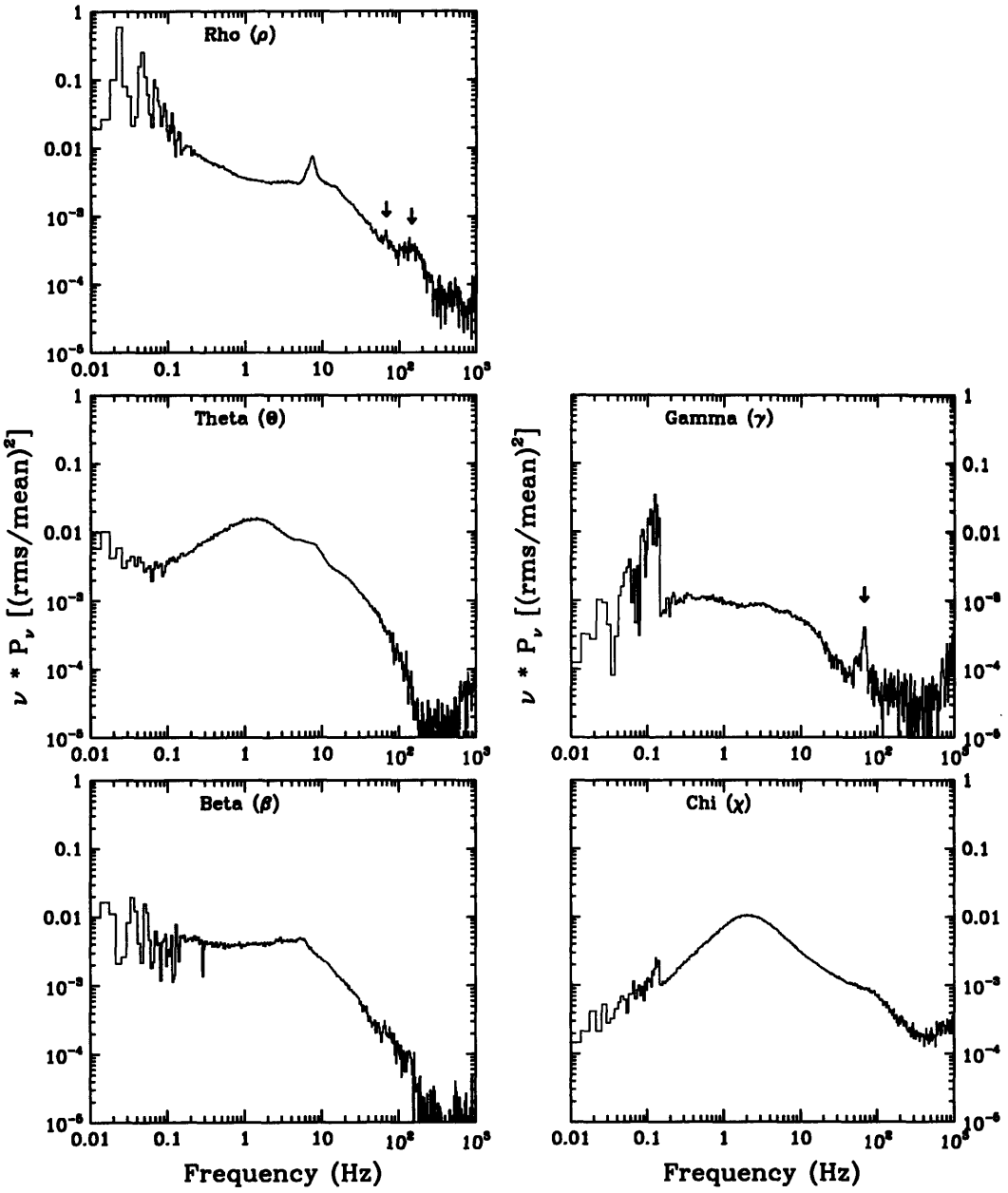

Figure 2-5: Five power-density spectra (medium-hard band: 6-30 keV) of GRS 1915+105 illustrative types of X-ray light curves.

2.5 Quasi-periodic Oscillations in GRS 1915+105

2.5.1 67 Hz QPO

The 67 Hz QPO excited by GRS 1915+105 is of particular interest to astronomers. Unlike other HFQPOs detected in BHB systems, the GRS 1915+105 67 Hz QPO can

be excited in a thermal spectral state. Generally, high frequency QPOs are observed to occur during a spectral state where the disk competes with a steep power-law spectrum.[13] The physical origin of the steep power law is unknown. However, the physics governing the thermal accretion disk has been modeled and fit to the thermal X-ray component with great success as a disk blackbody. Therefore, a thermal QPO is of particular importance to understanding the nature of QPOs.

In certain steady observation classes (particularly the γ class), the 67 Hz QPO is observed to radiate with relatively large power (greater than 2% of the rms power compared to $\leq$1% for other HFQPOs). When entire observations of variable emission are studied, many types are void of the 67 Hz QPO. The main goal of this study, dividing a variable observation class into phase bins of the variability cycle, is pursued in hopes of exposing a more significant 67 Hz QPO in a fraction of the entire variability cycle. Variable observations present conditions where the energy flux and spectra of the source change drastically within seconds. A situation where one fraction of the phase excites a 67 Hz thermal QPO and the surrounding phase fractions do not offers hope of gaining insights as to what causes the QPO and how quickly the QPO responds to spectral changes.

2.5.2 Power Law QPOs

HFQPOs of other BHBS are associated with the SPL state.[14] Higher frequency QPOs have been detected in the observations of GRS 1915+105 at 113 and 168 Hz. These HFQPOs are seen in the ν-type and θ-type light curves, respectively, when the X-ray colors and LFQPO properties of GRS 1915+105 indicate that the source is in the steep power law state. A broad 153 $\pm$ 8 Hz QPO (marked in the ρ panel of Figure 2-5) is suggestive of the θ-type 168 Hz QPO, and may also respond to dividing the ρ variability cycle. Because certain variable observation classes may excite both the 67 Hz QPO and higher frequency QPOs, this study hopes to identify

[13]McClintock, J.E., and Remillard, R.A., "Black Hole Binaries." 2003. p. 24.[12].

[14]Remillard, R.A. and McClintock, J.E. "X-Ray Properties of Black-Hole Binaries" 2006. p. 65.[11].

such opportunities.

A general quality of QPO excitation is that GRS 1915+105 (or any BHB) does not excite two QPOs simultaneously. Dividing variable oscillations (where the entire cycle excites two QPOs) into phase intervals will provide another test for this assumption. Furthermore, the rapidity by which such variable classes oscillate between spectral states may provide additional insight into links between QPOs of differing frequency.

Chapter 3

ρ-Type Variability Cycles in GRS 1915+105

Belloni et al. (2000) outline a classification system for the different patterns of X-ray variability seen in GRS 1915+105. The ρ class is defined as follows:

> Taam et al. (1997) and Viulhu & Nevalainen (1998) presented extremely regular RXTE light curves of GRS 1915+105, consisting of quasi-periodic 'flares' recurring on a time scale of 1 to 2 minutes ... class ρ is extremely regular in the light curve, and in the [color-color diagram] it presents a loop-like behavior.[1]

The description is paired with a plot like Figure 3-1. The light curve appearance and the tracks on the color-color diagram form the basis for the classification scheme for the twelve GRS 1915+105 classes. To understand the ρ cycle, however, requires a far more in depth study.

In this chapter, 82 ρ observations with RXTE[2] are analyzed to achieve a full picture of the ρ observation class and it's "extremely regular" but also extremely variable cycle. We begin with a basic description of the ρ light curve and color properties, which will be used to describe one motivation for selecting the ρ class, i.e.

[1] T. Belloni, et al. A model-independent analysis of the variability of GRS 1915+105.[1].
[2] Identified by R. Remillard

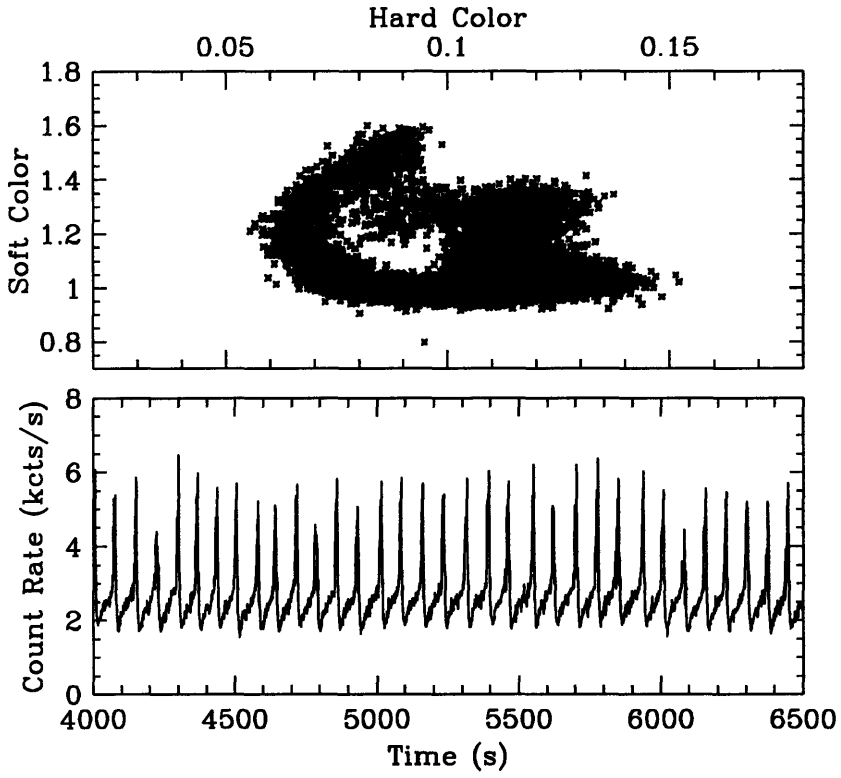

Figure 3-1: A color-color diagram atop a 3500 second light curve of ρ observation day 1053.

a connection to spectral characteristics associated with the QPO at 67 Hz. Next, we use the flare amplitude and recurrence time to define distributions within the ρ class. A scheme for dividing the 82 observations into three sub-classes is outlined, and the results discussed. Finally, QPO measurements averaged in phase bins within the ρ cycle are presented for all 82 observations, and again for each sub-class.

3.1 The ρ Cycle and Motivation for Investigation

Developing an in-depth picture of the ρ observation class begins with the basic ρ light curve which was shown in Figures 2-1 through 2-3. We show a 200 second ρ light curve in Figure 3-2 as we begin to examine the ρ cycle in further detail.

While obviously highly variable, the ρ cycle is astonishingly repetitive, and the

source appears to oscillates over the same path in spectral evolution during each cycle. In the same paper outlining a classification system for GRS 1915+105, this idea of movement between three distinct emission modes is described as a disk-instability model,[3] and the ρ cycle can also be investigated from this point of view.

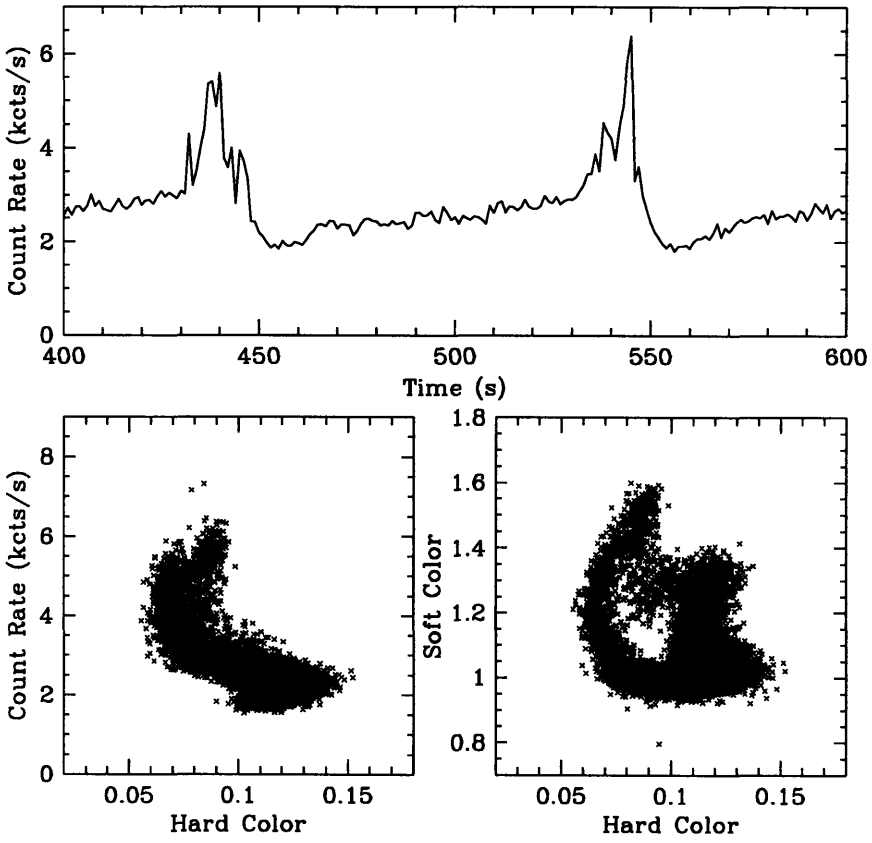

Figure 3-2: A 200 second light curve of ρ observation day 1053, showing the fine structure that is often present in individual ρ-type flares. The color-color and color-intensity diagrams cover the entire observation exposure time.

Broad band light curves are rarely plotted alone. One reason for this is a loss of information due to summing X-ray counts of different energies, which effectively washes out any spectral information. In Figure 3-2, two additional plots below the light curve track the spectral changes associated with the rapid changes in total X-ray counts. This is achieved by dividing the total counts into three energy bands: A, B,

[3]T. Belloni, et al. A model-independent analysis of the variability of GRS 1915+105.[1].

and C (2-5, 6-12, and 13-50 keV, respectively). The color-intensity diagram (left) plots hard color (C/B) vs. count rate, and the color-color diagram (right) plots hard color vs. soft color (B/A). The combination of these two plots provides information on how the "color" of the X-ray emission is changing as well as a link between color and the intensity of the emission.

Classically, color-intensity diagrams are plotted with X-ray counts against hard color. This choice is made because the soft color is strongly influenced by the amount of interstellar gas that lies along an observer's line of sight to an X-ray source, making soft color comparisons between different sources dependent on the source location. Furthermore, it has been shown that radio jets tend to occur only when observations occur above a particular value of hard color, so a color-intensity diagram using hard color can be used to diagnose observations that are in the hard state. For the ρ observations of GRS 1915+105 the color-intensity diagram with X-ray counts plotted against Soft color (henceforth soft color-intensity diagram) is of additional interest. The soft color-intensity diagrams of ρ observations, as in Figure 3-3, display a loop-like cycle similar to those seen in ρ color-color diagrams.

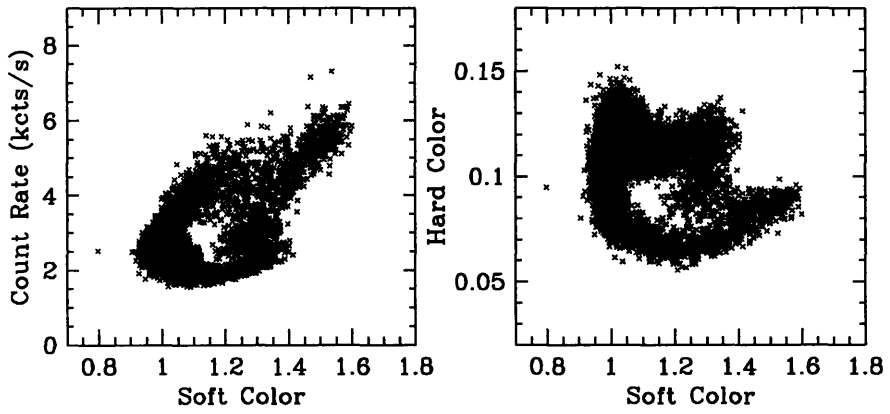

Figure 3-3: A soft color-intensity diagram (left) and color-color diagram (right) for ρ day 1053, showing that loop-like behavior occurs in soft color-intensity diagrams as well

3.2 Selecting the ρ Class

Only one of the twelve observation classes of GRS 1915+105 is targeted for study in this paper, the ρ (rho) class. The ρ observation class was chosen for three reasons, outlined below:

3.2.1 Characteristics of the ρ Class

Belloni et. al (2000) remarks that the ρ flaring cycle repeats on timescales from one to two minutes, during which the source also completes the color-color cycle. This study tries to answer some basic questions about the characteristics and behavior range of ρ cycles. Such properties include recurrence times (or cycle period) of ρ flares, flare fraction, amplitude, maxima, and width.

We list properties of interest and the calculated values in Table 3.1. Values given are minimum, maximum, mean ($/mu$) and standard deviation (σ_μ). The σ_μ represents the variation in the mean, and is not a statistical result–the standard deviations represent significant changes between individual flares and individual days.

Property	minimum	maximum	μ	σ_μ
cycle period	33.73	122.49	65.44	2.19
flare fraction	0.12	0.38	0.20	0.01
flare amplitude	1262.04	3598.71	2943.17	53.06
flare maxima	2191.89	5436.12	4414.56	64.13
flare width	8.33	45.80	13.33	0.51

Table 3.1: Results of studying the ρ-type observations of GRS 1915+105 in depth.

A number of these properties were found to correlate in interesting ways with the cycle period, including flare fraction, amplitude, and maxima. These correlations are discussed in section 3.3 as they apply to the idea of ρ sub-classes.

One unexpected result from this study was the great range in cycle periods for ρ observations. The initial paper laying out a classification scheme for observations of GRS 1915+105 described the ρ flares as "recurring on a time scale of 1 to 2 minutes."[4]

While a somewhat accurate prediction, the true range of ρ cycle periods as observed to present is between 36 and 126 seconds. This wide range of observed cycle periods, none of which appears as an outlier, covers a factor of greater than three in time space, and adds relevance to the study of ρ observations as three sub-types.

3.2.2 Periodic Variability Cycle

By studying thousands of ρ cycles one can determine, with superior statistics, the detailed and repeatable characteristics of this instability oscillation.

For observations that exhibit high variability, integrating over long exposures smears any spectral or intensity structure that may occur. A need to solve this problem becomes more compelling when an observation is not only variable but undergoes a periodic variability cycle. For observations of the ρ class, the variability cycle is clearly divided between double high-intensity flares of differing color followed by a period of low intensity emission, as is observable in Figure 3-2. The shape and nearly periodic nature of these flares has won the ρ variability cycle a nickname of "heartbeats." Because of the great variation between intensity of the heartbeat flares and low emission separating them, ρ offers an opportunity to separate different radiating modes which the GRS 1915+105 accretion disk oscillates between in a repeatable fashion. Such a separation would allow for long-exposure studies of a the average ρ variability cycle in discrete phase bins for different types of measurement quantities.

By phase resolving the ρ variability cycle, the goal of studying spectral evolution needed for emission models can be reached. Studying the ρ class in such detail also allows for the development of a standard toolset for analyzing data collected on any highly variable yet periodic emission type of any X-ray source.

3.2.3 Thermal Quasi-Periodic Oscillations

The variability and periodic nature of the ρ observation class further provides an opportunity to investigate high frequency QPOs of BHB systems. The class becomes

[4]T. Belloni, et al. "A model-independent analysis of the variability of GRS 1915+105."[1]

a near ideal candidate for study because there are signs of high frequency QPOs when the PDS are simply averaged over the entire variability cycle for all 82 RXTE observations, shown in Figure 3-4. The two high frequency bumps at 67 Hz and 150 Hz are significant detections, but the 67 Hz bump is weak.

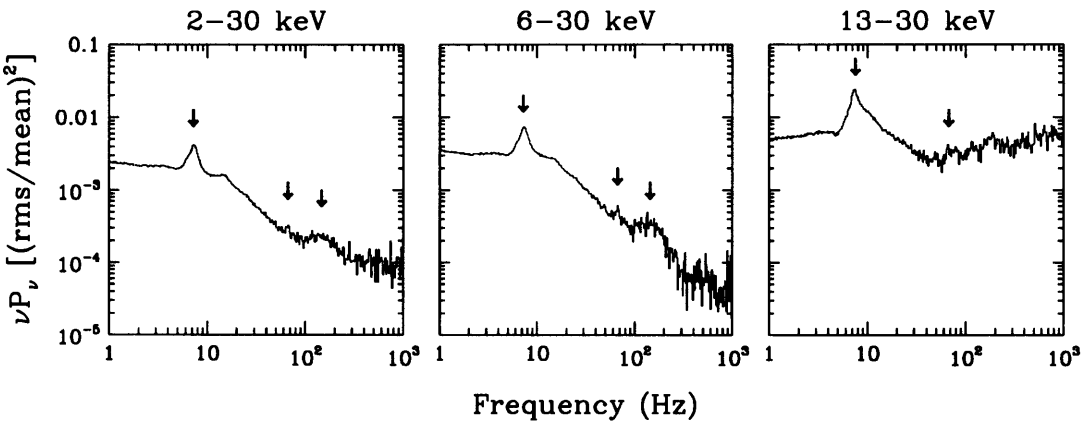

Figure 3-4: PDS in 3 energy windows of all 82 ρ observations averaged over the entire variability cycle. LFQPOs are noted by blue arrows, HFQPOS by red arrows.

Energy Band	ν	χ^2	Q	rms	σ_{fit}
2-30 keV	7.26	60.77	6.66	0.02362	215.25
2-30 keV	67.75	1.34	67.75	0.00165	2.57
2-30 keV	146.90	1.50	5.60	0.00397	4.42
6-30 keV	7.31	52.85	5.90	0.03434	225.79
6-30 keV	67.64	1.26	67.64	0.00275	3.50
6-30 keV	143.16	1.24	5.77	0.00560	4.11
13-30 keV	7.51	23.07	4.10	0.07856	155.46
13-30 keV	66.29	0.75	56.18	0.00721	2.12

Table 3.2: Significant HFQPO results for the averaged ρ variability cycle and all 82 observations. Two $< 3\sigma$ results are shown because of the 67 Hz QPO focus in this thesis.

One steady observation class of particular interest to the 67 Hz QPO is the γ (gamma) class, which is described as "relatively quiet," with "10 second quasi- periodic oscillations," and a "diagonally elongated" color diagram.[4] The average PDS of

[4]T. Belloni, et al. A model-independent analysis of the variability of GRS 1915+105.[1].

30 γ-class observations shows a QPO at 66.81 $\pm$ 0.21 Hz at 19.14σ in the sum band (2-30 keV). Table 3.3 includes QPO fitting results for all γ observations in 2-30 keV, 6-30 keV, and 13-30 keV bands.

Energy Band	ν	χ^2	Q	rms	σ_{fit}
2-30 keV	66.81	1.48	4.93	0.00511	19.14
6-30 keV	67.67	0.41	5.67	0.00686	13.42
13-30 keV	67.10	0.60	6.80	0.03139	12.13

Table 3.3: QPO significance results for the γ steady observation class.

We further illustrate the strength of 67 Hz QPOs in some γ-class observations by displaying PDS for three individual observations in Figure 3-5. A color-color diagram containing all of the gamma observations stacked on one another with the high QPO activity days, Figure 3-6, appears to localize particularly strong 67 Hz γ days to a small region of color-color space.

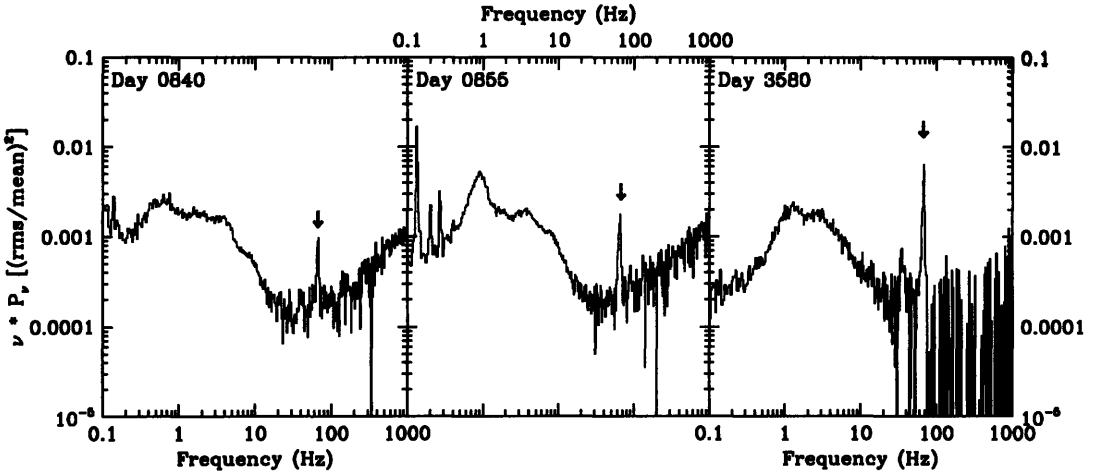

Figure 3-5: Fast-fourier transforms in three bands for each of three very strong 67 Hz QPO observations of type γ.

Fitting PDS of the ρ observation class exposes a QPO of far weaker power at 67 Hz (Table 3.5). The significance of this QPO is 3.50 σ in the 6-30 keV band, just powerful enough as a publishable result and with plenty power to draw attention. As earlier discussed, the averaging of the entire ρ variability cycle in which only a portion

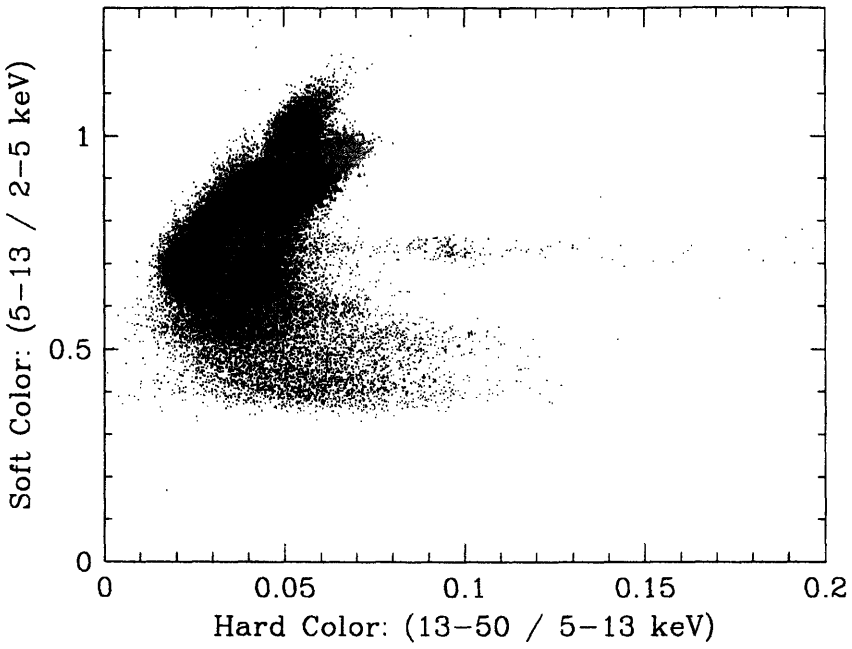

Figure 3-6: A color-color diagram presenting all γ data, with three very strong 67 Hz results in color: day 0840 (green), day 0855 (blue), day 3580 (red).

Observation	Energy Band	ν	χ^2	Q	rms	σ_{fit}
day 0840	2-30 keV	67.37	1.03	19.36	0.00829	15.30
day 0855	2-30 keV	65.24	1.14	17.12	0.01191	22.22
day 3580	2-30 keV	68.02	0.69	30.10	0.01930	30.80
day 0840	6-30 keV	–	–	–	–	–
day 0855	6-30 keV	–	–	–	–	–
day 3580	6-30 keV	67.97	0.66	27.08	0.02409	32.90
day 0840	13-30 keV	68.17	0.60	13.29	0.06917	3.84
day 0855	13-30 keV	65.21	0.58	16.02	0.05232	13.61
day 3580	13-30 keV	68.16	0.45	32.77	0.08010	13.59

Table 3.4: QPO significance results for three QPO significant γ steady observations.

of the phase excites a 67 Hz QPO would significantly decrease the measured power, simply as a matter of statistics. If one section of the ρ variability cycle excites the 67 Hz QPO while other phase slices do not, the significance of the QPO fit in the data limited to that phase will be higher. Isolating the phase zone that produces the 67 Hz QPO might also provide some insight to the QPO mechanism.

Energy Band	ν	χ^2	Q	rms	σ_{fit}
2-30 keV	67.75	1.28	67.75	0.00182	3.08
6-30 keV	67.64	1.28	67.64	0.00272	3.50
13-30 keV	66.32	0.78	56.18	0.00723	2.13

Table 3.5: QPO significance results for the entire ρ variability cycle.

A method of predicting which region of the ρ variability cycle might excite the 67 Hz QPO involves a comparison of the ρ color-color diagram to that of the γ color-color diagram. First, as in Figure 3-7, a "gamma-box" has been constructed around the three strongest 67 Hz QPO observations.

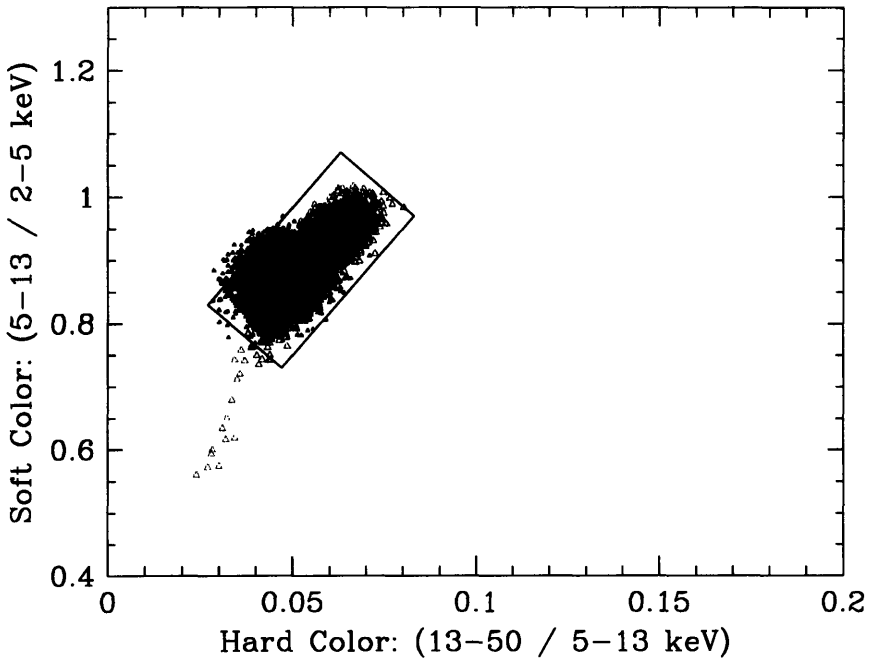

Figure 3-7: A color-color diagram presenting three very strong 67 Hz γ results in color: day 0840 is green, day 0855 in blue, and day 3580 in red. The plotted box serves as a reference for the γ occupation zone of color-color space.

Now, this gamma box is overlayed on a ρ color-color diagram in Figure 3-8. Doing so will show what section (if any) of the characteristic ρ color-color cycle lies in the same color zone as that of the QPO strong γ observations.

If this simple result is to be trusted, we would expect a sufficiently small fraction

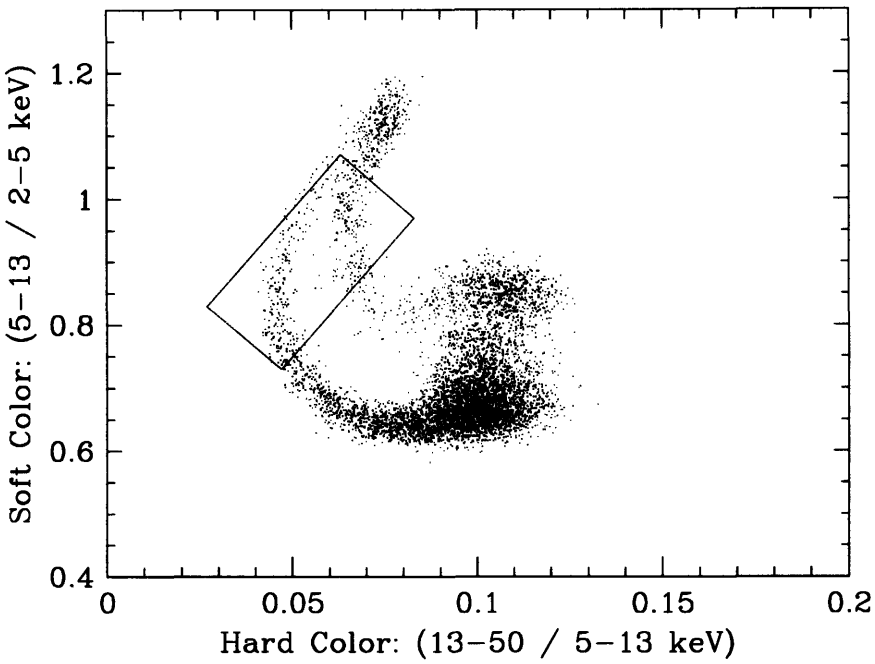

Figure 3-8: A color-color diagram of ρ day 1251a, overlayed with the gamma box established in Figure 3-8.

of the ρ variability cycle to excite the 67 Hz QPO which would greatly increase the 3.50 σ result of the entire cycle. One might also try to separate the two tracks of the ρ cycle through the gamma box, but variability among separate ρ observation days make such a study difficult.

3.3 Sub-Classes of the ρ Cycle

While examining the recurrence time distribution of the ρ cycle (Section 3.2.1) it became apparent that there was some correlation between the recurrence time and the flare profile. The qualitative differences appeared significant enough to warrant finding a quantitative way to investigate this and to define sub-classes for the ρ cycle. Finding a division criterion is a topic that must precede the effort to divide the ρ variability cycle into phase bins for power density and energy spectral studies, since this process should then be done by sub-class, not as a global method.

3.3.1 Qualitative Division

Studying the light curves and color-color cycles of many individual ρ observations revealed three "shapes" of color-color cycles all containing the distinctive ρ loop, but differing from one another enough to warrant further attention. Figure 3-9 shows examples of these three ρ color-color loop types, each overlapped by the γ box.

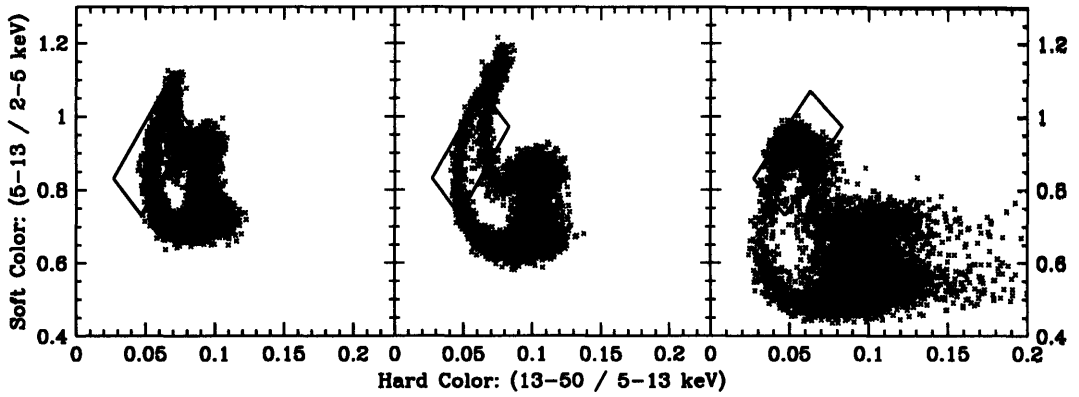

Figure 3-9: The three proposed sub-classes in color-color space with the γ 67 Hz QPO activity box first plotted in Figure 3-7. Notice that the γ box covers a region in the ρ color-color diagrams where the three types differ most. Left (ρ_1): day 1053, center (ρ_2): day 1251a, right (ρ_3): day 2362.

Figure 3-9 suggests that a ρ sub-class division may be important to 67 Hz QPO excitation. The region of the ρ color-color cycle which differs the most in each sub-class coincides with that region which passes through the γ occupation region. If color-color space is indeed a criterion for exciting the 67 Hz QPO, we expect to see a difference in the strength or very ability of different sub-classes 67 Hz QPO excitation.

Separating ρ observations into useful subclasses was attempted with a number of parameters. These chosen parameters were based on qualitative study of ρ observations. The study suggested that timescale between flares would be of importance, as well as the number of X-ray intensity peaks per flare, the width of the flares, the form of the color-color loop, and color properties of the flares. Physical properties based on these observations were selected for qualitative study.

3.3.2 Quantifying Sub-Class Division

Extensive analysis on the 82 ρ light curves and PDS allowed the collection of a large number of interesting parameters, including:

1. Cycle Period: The length of the variability cycle, or time between successive flares. This data was extracted from PDS of ρ observations, as the ρ cycle itself can be seen as a very low frequency QPO.

2. Flare Fraction: fraction of an observation's exposure with a count rate greater than 20% above the mean count rate of the entire observation. An indicator of the percentage of time an observation spends in flaring mode.

3. Flare Width: Seconds per flare.

4. Flare Count Rate: The average count rate per flare.

5. Minimum, Mean and Maximum Count Rates

6. Occupation of γ box: The fraction of time any single observation day spends within the γ box discussed in section 3.2.3

After investigating different options, two parameters were used to divide the 82 ρ observations into three sub-classes. The two parameter plane of flare fraction plotted against cycle period, Figure 3-10, was chosen because it provided a two-track path through the parameter space which could be discussed in physical terms greater than the qualitative introduction in section 3.2.1.

This combination of parameters well fits what should be expected to divide the three sub-classes. Simple qualitative looks at ρ_1 observations indicated longer cycle periods, a quantity which well divides the ρ_1 observations from ρ_2 and ρ_3, while leaving the latter two sub-classes mixed. Where ρ_2 and ρ_3 groups differ is in the width of the flares, which well translates into flare fraction when considering that the two sub types appear to have indistinguishable cycle periods.

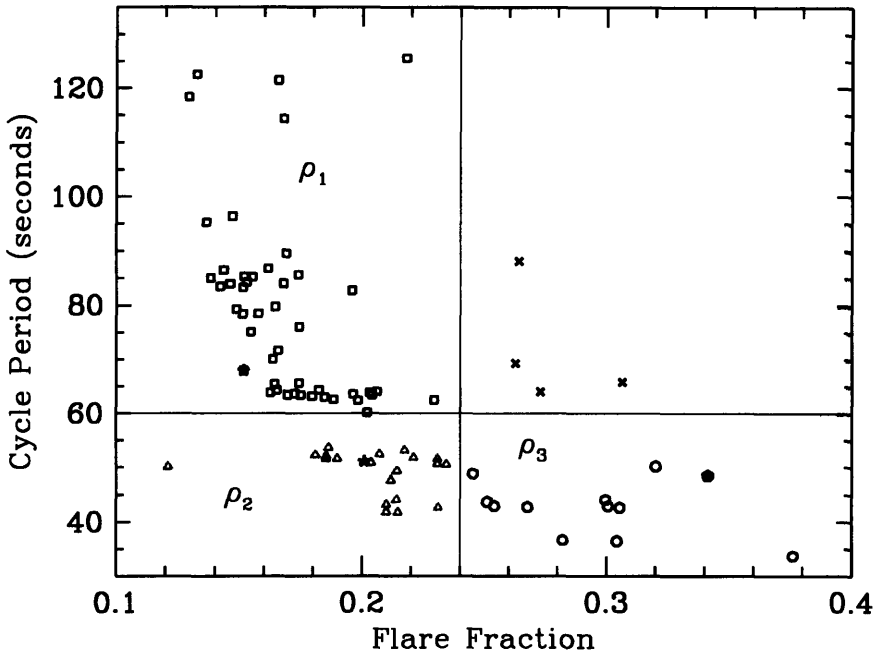

Figure 3-10: Parameter plane used to quantitatively divide ρ observations into sub-classes. The color and shape of points representing the different sub-classes is set here and used in later plots to determine the location of the observations in this plot. In each group, the point with a star in the center represents the template day. Red squares: ρ_1 observations; green triangles: ρ_2 observations; blue circles: ρ_3 observations; black "x"'s: four outliers.

The flare fraction vs. cycle period plane (Fig. 3-10) basically shows two tracks which meet at ρ_2. In the ρ_1 track, the decrease of cycle period, the time between successive flares, may be matched with a slight increase in flare fraction. In the ρ_2 zone, the decrease in cycle period comes to a stop–and the flare fraction begins increasing. ρ_3 observations continue this trend. The two-track evolution of ρ observations suggests that differences between sub-classes may be tied to the mass accretion or rate. This idea is developed fully in Section 3.3.4.

3.3.3 Sub-class definitions

In Figures 3-11, 3-12, and 3-13, prototype observations chosen for Figure 3-9 are further characterized with a sample 200 second light curve, a color-intensity diagram,

and a soft color-intensity diagram. These observations will serve as templates for phase-resolved analyses of the ρ cycle, and their locations in Figure 3-10 are shown with a star symbol.

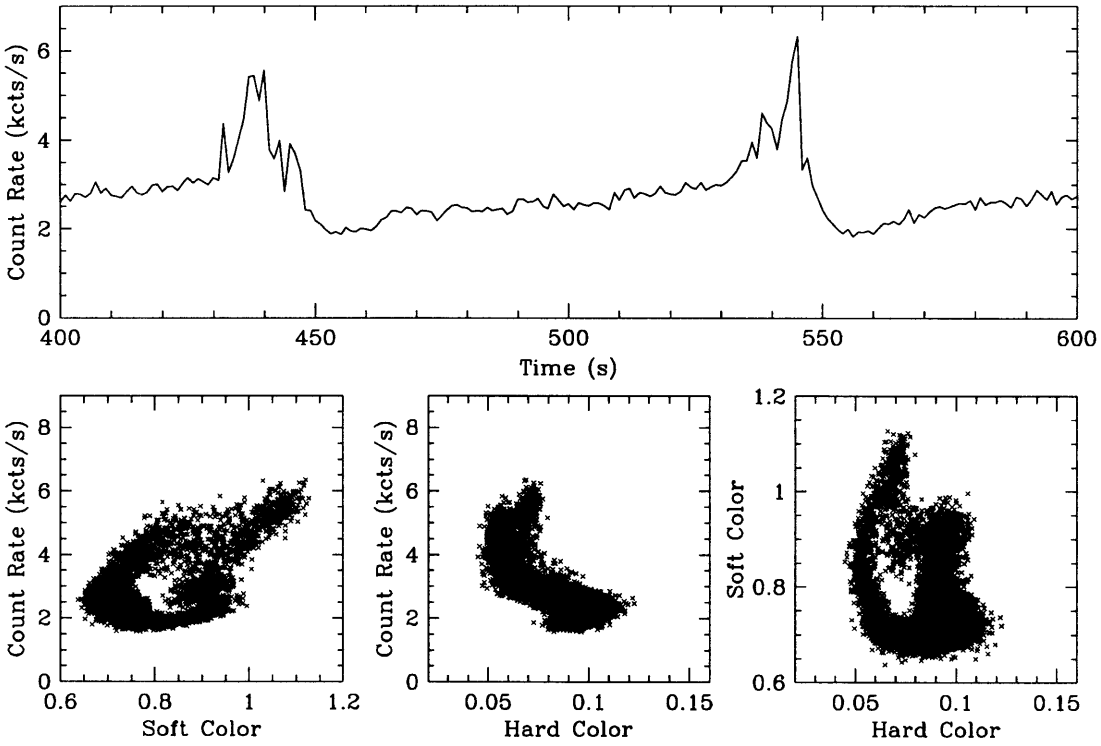

Figure 3-11: Day 1053, ρ_1 template. ρ_1 has long flaring periods with three or more peaks per flare. The time between flares is longer than in other sub-types. The color-color region of high soft color and low hard color appears muted, creating a tighter color-color cycle.

Observations of type ρ_1 are defined to have cycle periods greater than or equal to 60 seconds, and flare fractions of less than 0.24. There are 49 of the 82 ρ observations in the sub-class ρ_1, representing 54% of the total ρ exposure time in our RXTE sample. The ρ_1 sub-class covers the range of cycle periods presented by Belloni and his team, leaving nearly half of the ρ exposure time below this range.

Observations of type ρ_2 are defined to have cycle periods less than 60 seconds and flare fractions less than 0.24. The actual range is 40-55 seconds. The flares are narrow, covering less than 25% of the total exposure time. On average, ρ_2 observations do have higher flare fractions than ρ_1 observations (Figure 3-10). The ρ_2 observation

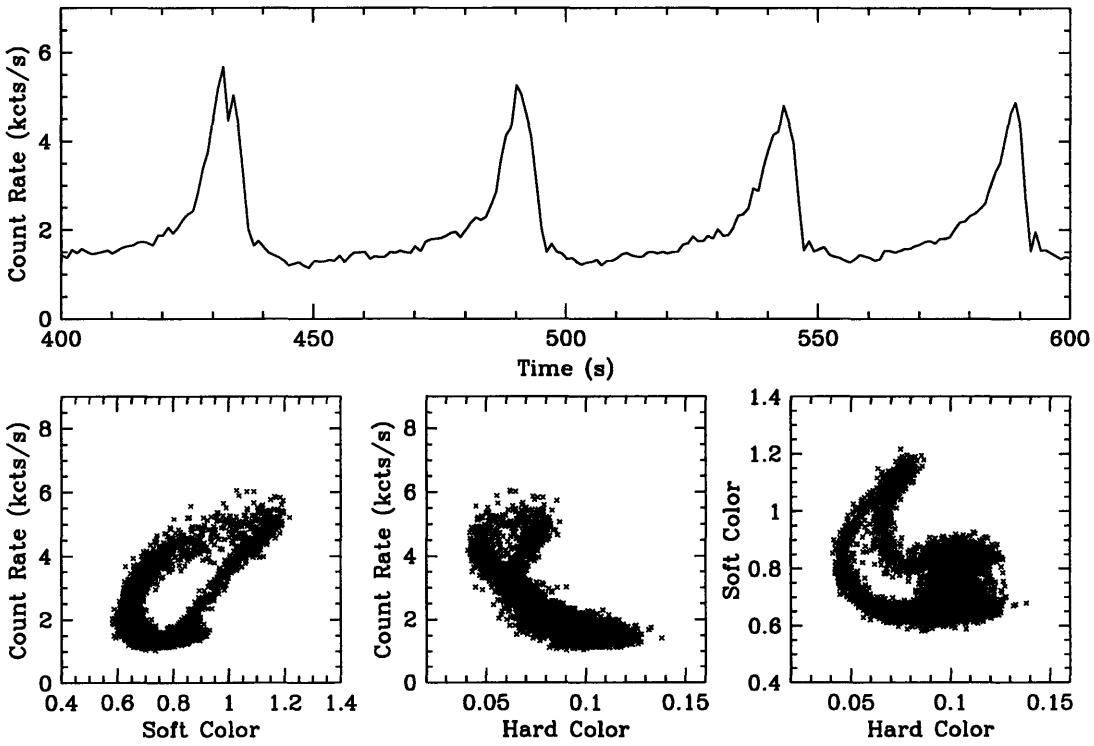

Figure 3-12: Day 1251a, ρ_2 template. ρ_2 has short flares with one or two discernable peak. The time between flares is significantly shorter than ρ_1 observations. The color-color diagram region of high soft color and low hard color reaches out farther from the double lobed, high hard color portion of the cycle than the other sub-types.

group contains 21 observations and represents 31% of the total ρ exposure time.

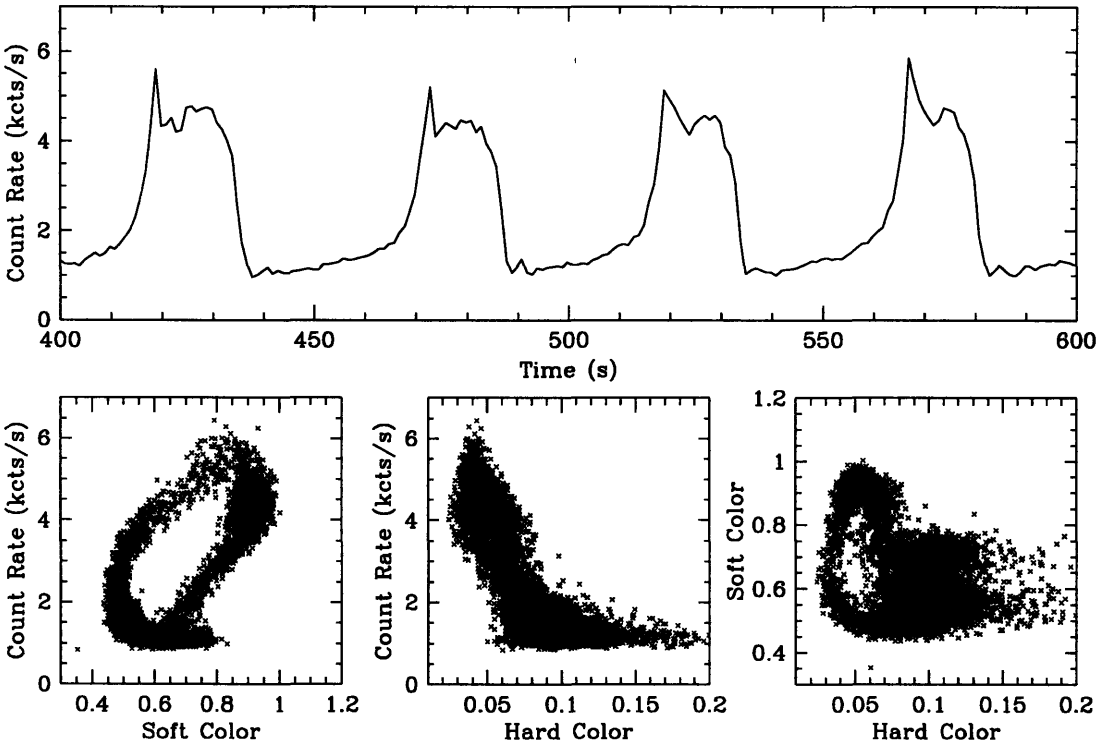

Figure 3-13: Day 2362, ρ_3 template. Long flares with sharp soft (first) peak followed by a broad, plateau-like hard peak. Time between ρ_3 flares is short. The color-color region of high soft and low hard color corresponding to the ρ flares is less sharp and more densely populated than ρ_1 or ρ_2 days.

Observations of type ρ_3 are defined to have cycle periods less than 60 seconds and as short as 36 seconds. Flare fractions of ρ_3 observations are greater than 0.24 and reach as high as 0.38, meaning that along with flaring quite rapidly, ρ_3 observations can flare for nearly 40% of their total exposure times. 12 of the ρ observations in this study are of type ρ_3, and the sub-class represents just over 15% of the total ρ exposure time.

Comparing the three sub-class template days against the first qualitative suggestions of sub-classes (see Fig. 3-9) strengthens the claim that significant physical differences may exist in the ρ class. The two-track evolution of the ρ cycle through flare fraction vs. cycle period space (see Fig. 3-10) provides motivation to conduct further analyses to explain physical conditions of accretion in the GRS 1915+105

system that might differentiate the ρ sub-classes.

3.3.4 Physical Meaning of ρ Sub-Classes

Because the fastest cycling times also correspond to the longest and most steady flares, the physical mechanism that might distinguish ρ sub-classes is the mass accretion rate, dM/dt. The idea behind this proposed mechanism is that ρ flares occur more frequently and with longer duration when more material is accreting. Figure 3-10 does show what could resemble a dM/dt curve, starting at the longest ρ_1 cycle periods and increasing through the ρ_2 and into the ρ_3 zone. One could speculate that the instability cycle itself is limited to timescales of ≤ 40 s, i.e. the characteristic value for regions ρ_2 and ρ_3, so that further needs to release energy create larger flares rather than faster recurrence times. Then in the ρ_2 and ρ_3 regions, the value of dM/dt during the flares may be approaching the Eddington limit, in which flares can not get any brighter, but instead are lengthened and flattened into the plateau characteristic of ρ_3 flares.

One simple way to test this is to look at the mean count rate of entire observations, in which the dM/dt should surface. However Figure 3-14 does not display a trend that would confirm a dM/dt cause for the different sub-classes. This topic can be reexamined with spectral fits to use integrated energy flux rather than the PCA count rate, which is only a loose proxy for mass accretion rate.

We next examine the flare amplitude of the ρ cycle vs. sub-class and cycle period in Figure 3-15. The error bars in Figures 3-15 and 3-16 are sample standard deviations, and represent changes in the flaring data, not simply statistical values. The apparent flare amplitude saturation around 3500 cts/s/PCU is interesting and this suggests some kind of limit to the energy release in the flare associated with the ρ process. One type of limit is the Eddington limit, where radiation pressure forces a maximum value of dM/dt. This process requires an absolute boundary for X-ray emission not a flare amplitude. Figure 3-16 tests this, and while the sharpness of any count rate maximum is debatable, we can suggest a maximum of 5000 cts/s/PCU and assess this limit in terms of the Eddington luminosity, L_{Edd} of GRS 1915+105. While the 5000

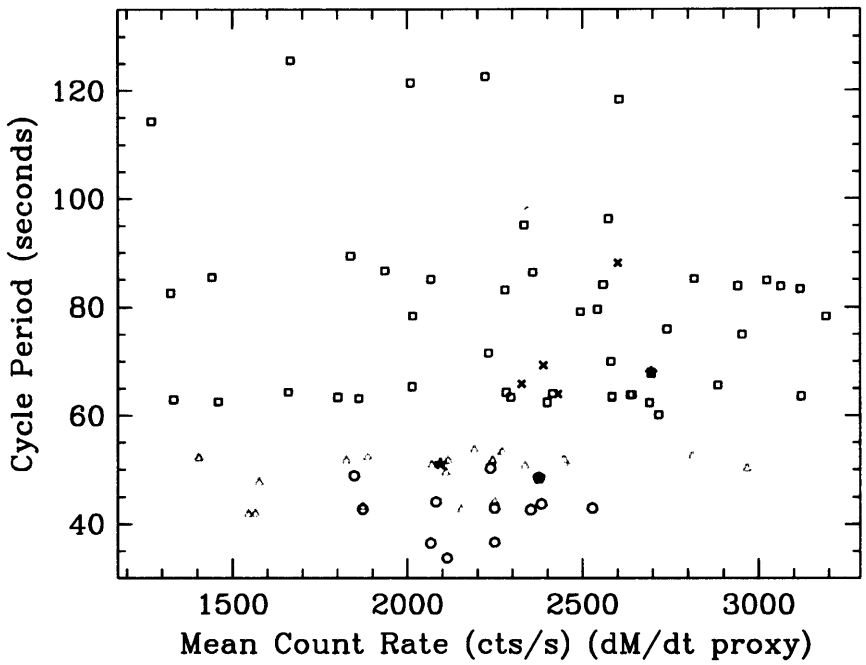

Figure 3-14: Cycle period plotted against mean count rate. Mean count rate is used here as a proxy for dM/dt, or the mass accretion rate. The plot shows that dM/dt is not the mechanism for the ρ flaring cycle, or that mean count rate is not a good proxy for dM/dt. Red squares: ρ_1 observations; green triangles: ρ_2 observations; blue circles: ρ_3 observations; black "x"'s: four outliers.

cts/s/PCU does not show as a sharp limit in Figure 3-16, using a sum band count rate to estimate luminosity can diverge from full spectral energy fits by as much as 20%.

$$L_{Max} = f_{abs} * \frac{5000}{2500} * 5.0x10^{-8} * 4\pi d^2 = (1.87 \pm .43)x10^{39} * f_{abs} \left[\frac{erg}{s}\right] \qquad (3.1)$$

The process begins with scaling GRS 1915+105 count rates to Crab units (2500 c/s/PCU = 5.0x10^{-8} erg/cm^2/s at 1-30 keV), and requires the addition of a scaling factor f_{abs} (>1) to account for the suppression of GRS 1915+105 raw count rates by photoelectric absorption in the Milky Way. We define Equation 3.1, with d representing the distance to GRS 1915+105 (12.5 $\pm$ 1.5 kpc) in centimeters. The error

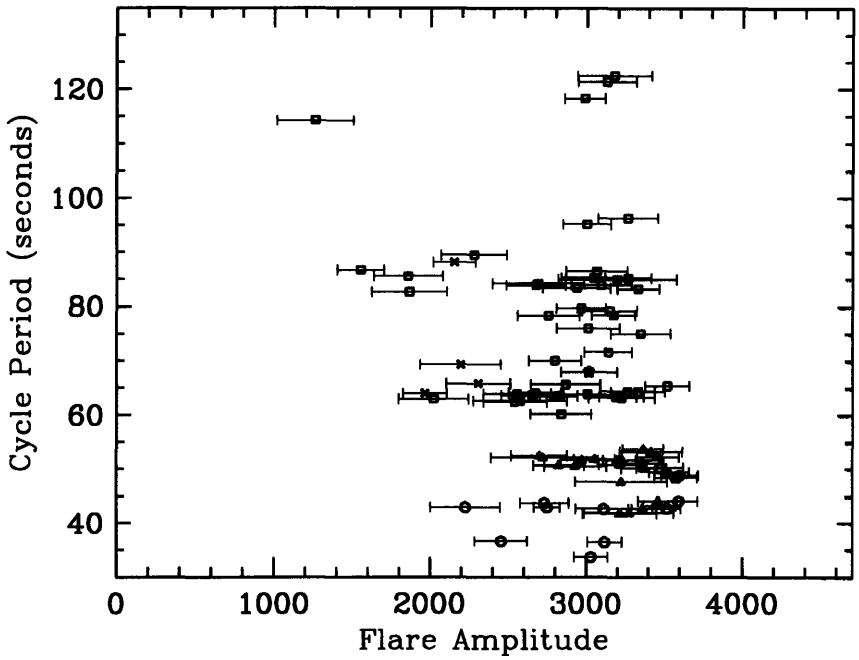

Figure 3-15: Note the saturation of flare amplitude at ~3500 cts/s/PCU independent of cycle period.

bar on this value of L_{Max} is propagated from the error in the estimate of d and a 20% error to cover both the the choice of where to draw the count rate limiting line in Figure 3-16 and the conversion of that count rate into a flux.

$$L_{Edd} = 1.3x10^{38} * (M/M_{\odot}) = (1.82 \pm .52)x10^{39} \left[\frac{erg}{s}\right] \tag{3.2}$$

Equation 3.2 describes the theoretical Eddington limit of an accreting body for GRS 1915+105, where M = 14 ± 4 $M_{\odot}$.[6] To compare L_{Max} and L_{Edd}, we first rewrite L_{Max} to include an exact value of f_{abs} in the measurement of error, L_{Max} = f_{abs}*1.87x10^{39} ± f_{abs}*0.43x10^{39}. We estimate f_{abs} by performing spectral fitting on a sample of RXTE GRS 1915+105 data. After assuring a good fit, we integrate from 1-30 keV to estimate flux, then change the absorption coefficient to zero. Recalculating the flux from 1-30 keV with no absorption gives an overestimation of the flux. We estimate f_{abs} = 1.68 as the ratio of the flux without absorption to the flux with

[6]Greiner, Cuby, and McCaughrean. "An Unusually Massive Stellar Black Hole in the Galaxy." Nature, 414, 522. 2001.[4].

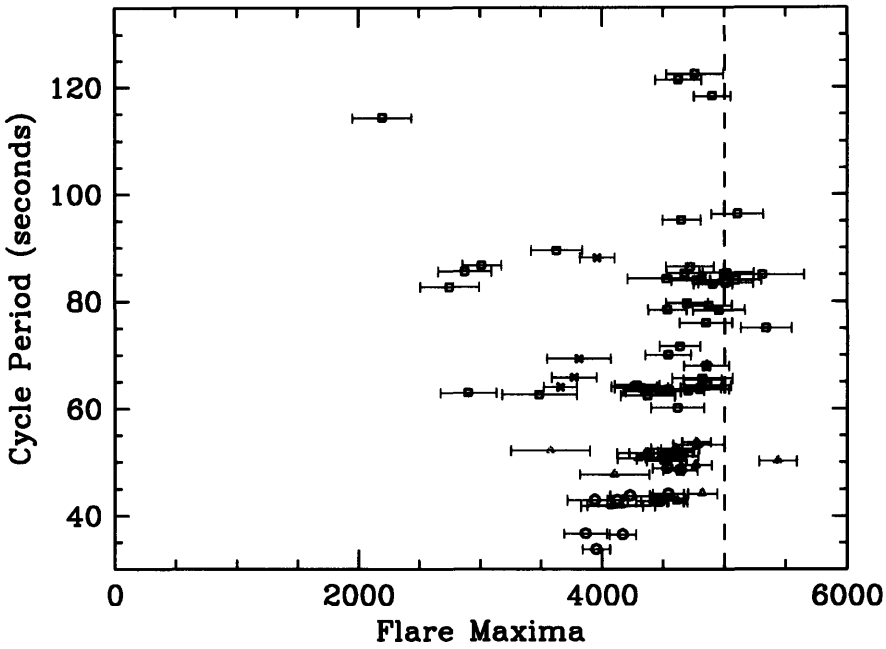

Figure 3-16: Possible absolute maximum count rate cutoff displayed with dashed red line at 5000 cts/s/PCU, independent of cycle period.

absorption. Using this estimate, we calculate the difference between L_{Edd} and L_{Max} in Equation 3.3:

$$L_{Edd} - L_{Max} = (-1.32 \pm .90)x10^{39} \tag{3.3}$$

Equation 3.3 indicates an L_{Max} which is greater than L_{Edd}, although only at 1σ. Within 2σ, the difference is negligible. While a result claiming that GRS 1915+105 radiates above the Eddington limit must be incorrect, we keep in mind that Equation 3.2 is a minimum value of the Eddington limit. The L_{Edd} calculated here is likely lower than the actual L_{Edd} of GRS 1915+105 due to a number of factors, including non-isotropic radiation and accretion material composed of hydrogen and heavier elements.

We acknowledge that there are a number of assumptions and uncertainties in any claim that the Eddington limit affects the ρ cycle and causes the ρ_3 sub-class to have high values in the flare fraction parameter (see Figure 3-10). These assumptions

include that a sharp value of maximum count rate limits the flare amplitudes of ρ observations (see Figure 3-16), that count rate may be used to estimate luminosity without full spectral fitting, and that an estimated $f_{abs} = 1.68$ adequately describes photoelectric absorbtion between GRS 1915+105 and RXTE. Further spectral fitting beyond the range of this thesis may be used to test these assumptions. Nevertheless, we note that the results of this study do suggest that the Eddington limit may be important to the ρ flaring mechanism, and may drive the increasing flare fractions of ρ_3 observations while the mechanism limiting cycle periods to >35s remains unknown.

3.3.5 Average Sub-class QPO results

One main reason for defining the ρ sub-classes was in response to differences in the color-color diagrams, particularly in the region of a γ box meant to specify a region of color-color space where GRS 1915+105 exhibits powerful QPOs at 67 Hz.

Studying PDS of the ρ observations summed by sub-class verifies significant differences in the strength of the 67 Hz QPO. Table 3.6 lists the QPO fits of the three ρ sub-classes in three energy bands. To understand these results as compared to the results for all ρ observations summed together (Table 3.5), we have selected the 6-30 keV band for a discussion of the statistics and expected results for a theoretical ρ class where sub-classes have no effect on 67 Hz QPO excitation.

Sub-class	Energy Band	ν	χ^2	Q	rms	σ_{fit}
ρ_1	2-30 keV	no QPO	–	–	–	–
ρ_2	2-30 keV	66.86	0.61	33.95	0.00320	4.14
ρ_3	2-30 keV	65.94	0.47	11.58	0.00361	3.08
ρ_1	6-30 keV	no QPO	–	–	–	–
ρ_2	6-30 keV	66.89	0.89	16.97	0.00371	3.38
ρ_3	6-30 keV	66.25	0.38	20.23	0.00713	3.85

Table 3.6: QPO significance results for each ρ sub-class in each of three energy bands.

When all 82 ρ observations are fourier-transformed and the resulting PDS studied, a 3.50σ QPO is fit at 67.62 Hz. Utilizing the sub-class divisions developed here, 54% of that data corresponding to ρ_1 observations did not excite enough of a 67 Hz QPO

to be detected. Assuming that all ρ data contributes equally to the 3.50σ result, or that every ρ observation excites the 67 Hz QPO with the same power, taking 54% of that data and re-fourier transforming that data should yield a QPO of 2.55 σ, which is on the verge of detectability but would not result in a null fit. This value is determined by a simple application of Poisson statistics, where the QPO signal depends on the square root of the observation exposure. Thus, the expected power for 54% of the data is determined by the equation: $3.50^{*}\sqrt{.54} = 2.55$.

Applying this method to the other sub-classes yields these expected results: ρ_1: 2.55 σ, ρ_2: 1.93 σ, ρ_3: 1.34 σ. Compare this to the actual results for the 6-30 keV band, tabulated in Table 3.6: ρ_1: null result, ρ_2: 3.38 σ, ρ_3: 3.85 σ. These results imply that not all ρ observations days produce the 67 Hz QPO equally. Instead ρ_1 observations appear to be very weak in terms of producing the 67 Hz QPO, while ρ_2 and ρ_3 observations more efficiently excite this oscillation.

This result adds another dimension to the differences between the ρ sub-classes proposed in this paper. As the differences between ρ sub-classes are limited (and easy to overlook), the possible physical mechanisms causing the 67 Hz QPO can be investigated via the differences between ρ_1 and ρ_3 observations. This idea will be further studied as a method of phase-separating the ρ variability cycle is developed in Chapter 4.

Chapter 4

Phase Binning the ρ Cycle

4.1 Phase Zones for the ρ Variability Cycle

Previous studies on the θ observation class of GRS 1915+105 (See Figure 2-3) show that QPO detections in variable observation classes may be isolated by studying phase intervals independently.[1] In such a situation, the QPO detection is weakened by studying a PDS averaged over the entire variability cycle.

We apply this idea to the GRS 1915+105 ρ class by dividing the ρ variability cycle into four phase zones. In Section 3.2.1, the ρ cycle is displayed in terms of both X-ray color and intensity properties. The most natural method of selecting phase zones utilizes the evolution in both the X-ray intensity and color that are seen to repeat in each ρ cycle.

The source count rate is the straightforward quantity that separates flaring and quiet sections of the variability cycle. A Soft Color (5-13/2-5 keV) criterion is chosen as the best method of separating the hard and soft peaks of the flare. These two quantities are used to define four phase zones, starting with the zone expected to contain the strongest 67 Hz QPO detections and continuing temporally through the ρ variability cycle: Zone 1 (flaring and high soft color), Zone 2 (quiet and high soft color), Zone 3 (quiet and low soft color), and Zone 4 (flaring and low soft color).

[1] Remillard, R. and Muno, M. and McClintock, J. E. and Orosz, J. "X-ray QPOs in black-hole binary systems." 2002.[9]

A pair of numerical values for the phase zone definitions were selected for each sub-class (Table 4.1), based on the properties of the template observation days for each. Figures 4-1, 4-2, and 4-3 illustrate the result of phase binning template ρ_1, ρ_2, and ρ_3 observations, respectively.

Sub-class	Count Rate Boundary	Soft Color Boundary
ρ_1	2700	0.82
ρ_2	2500	0.80
ρ_3	2000	0.65

Table 4.1: Sub-class dependent markers for count rate and soft color used to phase bin ρ observations.

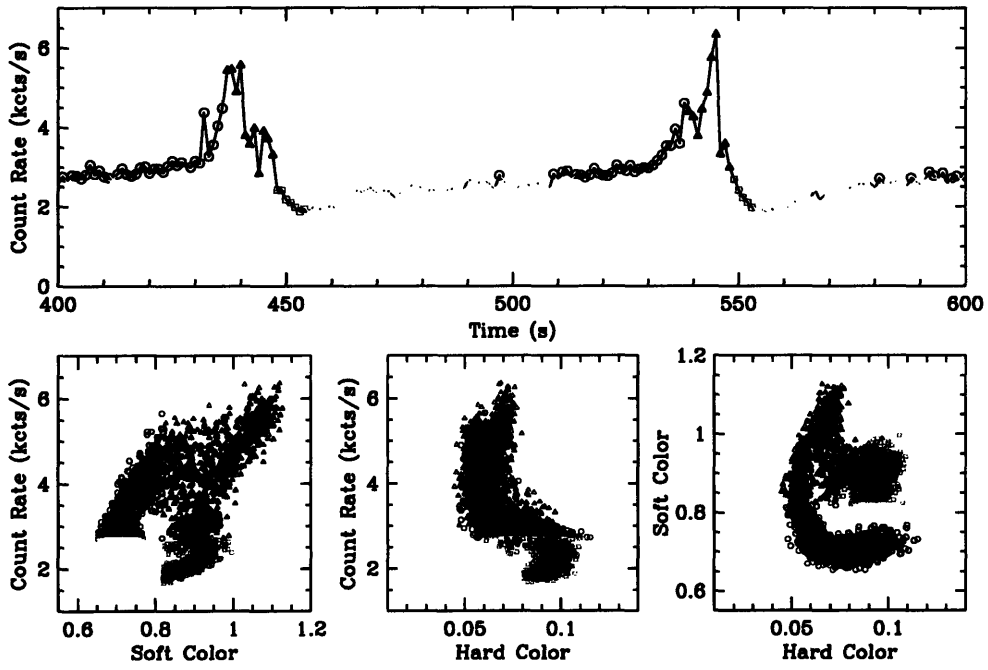

Figure 4-1: GRS 1915+105 observation day 1053, ρ_1 template. 200 second X-ray light curve with color-color and color-intensity diagrams representing the entire observation. Each representation of the observation is phase binned into four zones: zone 1 (blue triangles), zone 2 (green squares), zone 3 (yellow "x's"), and zone 4 (red circles).

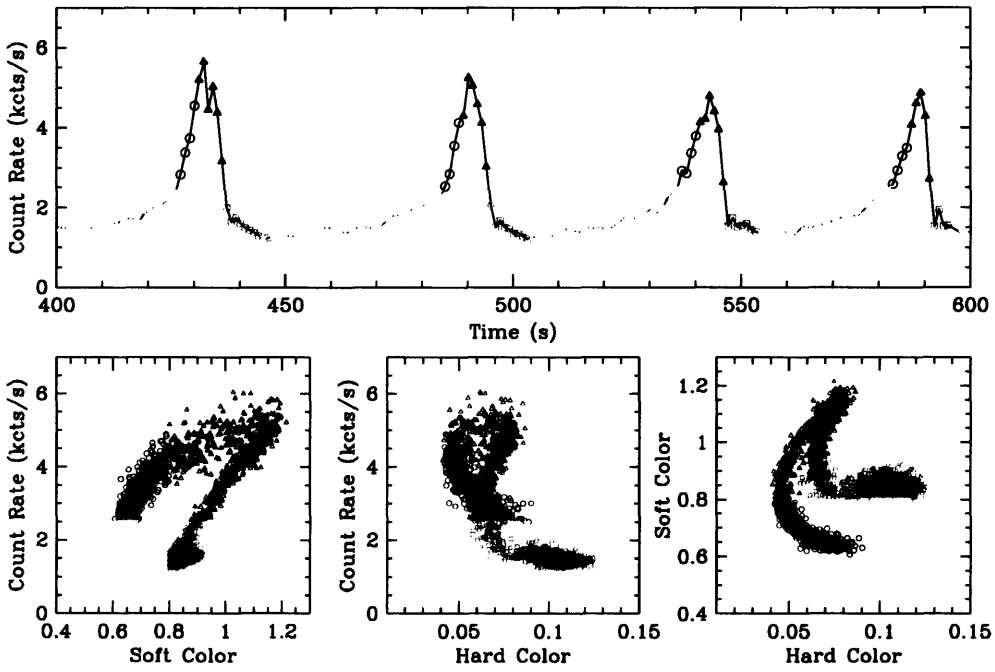

Figure 4-2: GRS 1915+105 observation day 1251a, ρ_2 template. 200 second X-ray light curve with color-color and color-intensity diagrams representing the entire observation. Each representation of the observation is phase binned into four zones: zone 1 (blue triangles), zone 2 (green squares), zone 3 (yellow "x's"), and zone 4 (red circles).

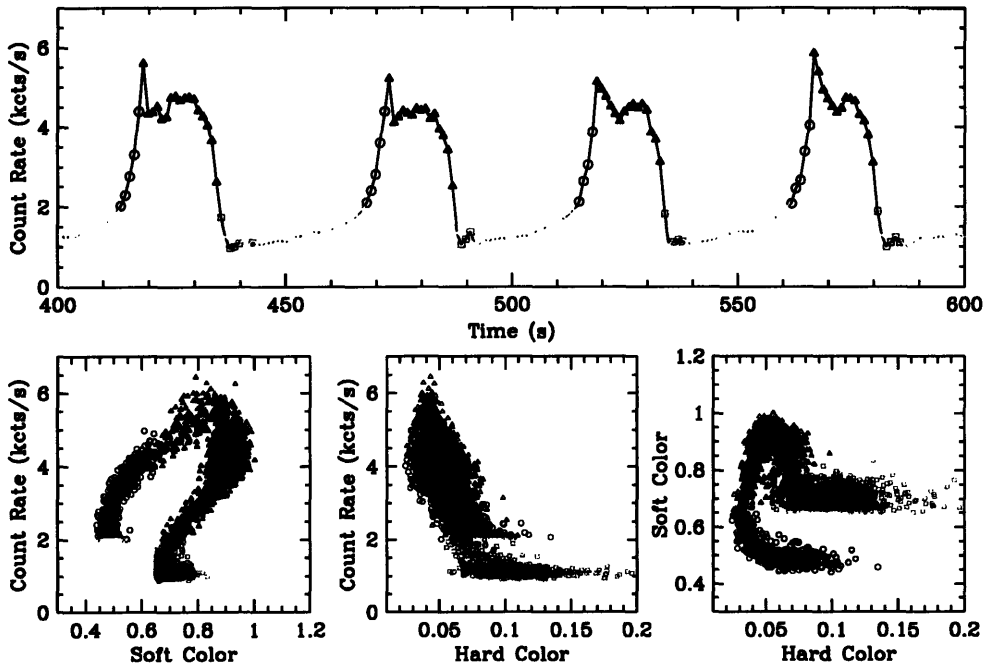

Figure 4-3: GRS 1915+105 observation day 2362, ρ_3 template. 200 second X-ray light curve with color-color and color-intensity diagrams representing the entire observation. Each representation of the observation is phase binned into four zones: zone 1 (blue triangles), zone 2 (green squares), zone 3 (yellow "x's"), and zone 4 (red circles).

4.2 Studying Power-Density Spectra

4.2.1 Extracting Information on Spectral State

Analytical techniques may be used to relate observations to the three states of black hole binary accretion defined by Remillard and McClintock 2006. The three states, thermal, hard, and steep power law (SPL) are discussed in Section 1.3.2.

In a situation where direct modeling of energy spectra is possible the spectra are deconvolved into disk-blackbody components plus a power-law component with photon spectrum, $N_{PL} \propto E^{-\Gamma}$. One may then distinguish separate states by the "disk fraction," or fraction of total flux (2-20 keV) which radiates as a thermal disk black body. For a thermal spectral state, this disk fraction will be $f > 75\%$. The hard state classification requires $f < 25\%$ and a $1.4 < \Gamma < 2.1$, while the SPL state has $f < 80\%$ with a $\Gamma > 2.4$.[1] The X-ray PDS is also used to define the spectral state. First, a measurement of the average integrated power from .1-10 Hz (calculated in the 2-30 keV energy window) is called the power continuum value, r (units are rms fraction), and observations in thermal states have low values ($r < .075$).[1] The SPL and hard states exhibit higher power density values ($r_{SPL} < 0.15$, $r_{hard} > .1$). An observation with a value of $.1 < r < .15$ might be hard, SPL, or a H:SPL intermediate state depending on the other criteria, i.e. the values of f_{disk} and Γ.[1] Second, any LFQPO activity (.1 - 30 Hz with rms amplitude > 0.005) dictates one of the nonthermal states.

As a substitute for full energy spectral analyses, values of hard color (C/B; 13-50/6-13 keV) are used to separate "soft" spectral states (thermal and SPL) from "hard" spectral states (hard or H and SPL intermediate). In GRS 1915+105, the state separator is defined with two lines on the color-color diagram: hard color = .06 for soft color values up to 0.8, followed by a linear increase to hard color = 0.8 at a soft color of 1.0 (Remillard, et. al., private conversation).

We can then estimate spectral states here by applying these three criteria. A

[1]Remillard, R.A. and McClintock, J.E. "X-Ray Properties of Black-Hole Binaries." 2006. p. 59.[11].

thermal state requires the following: a PDS with now LFQPOs, a PDS with r < .075, and a color-intensity diagram showing hard color below the state-discrimination lines defined above. SPL or thermal and SPL intermediate states show LFQPO detections, r < 0.15, and hard color again below the division lines. Hard states must show r > .1, and the hard color must be above the division lines in the color-color diagram. HFQPOs may be present in hard states.

4.2.2 QPO Fitting Parameters

QPOs are detected in PDS as Lorentzian profiles that improve the PDS models significantly when added to the power continuum background. The fits are done with χ^2_ν minimization, and the power continuum is modeled with a quadratic function in the plane of $\log(P_\nu)$ vs. $\log(\nu)$.[3] We consider $>3\sigma$ QPOs significant in this study, and $>4\sigma$ detections as strong.

The central frequency (ν) of a QPO locates the feature, and the full width at half maximum (FWHM) is used to define the coherence, Q = ν/FWHM. Coherence values of Q$\geq$2 distinguish QPOs from broad power peaks.[3]

In some cases, LFQPOs return high χ^2 values. Generally, high χ^2 fits for strong detections arise from three causes: LFQPOs may not be well represented by Lorentzian profiles, the fundamental QPO oscillation may be non-sinusoidal and produce PDS harmonics which are not well fit with Lorentzian profiles, or a QPO may be detected in a region where a continuum background has inflections or too much curvature. Harmonic LFQPOs and the fundamental feature are fit together, and tables of QPO fits will note the main harmonic at $2\nu_o$ when significant detections are made. LFQPO detections with χ^2>5 are studied on a case-by-case basis. In tabulated data, these QPOs are marked with the superscript "p" if found to be non Lorentzian profiles, and "c" if the continuum fit is poor.

The integrated QPO amplitude (rms) is a measure of the QPO power relative to the mean source count rate. LFQPOs help to define the X-ray state, as described in

[3]Remillard, R.A. and McClintock, J.E. "X-Ray Properties of Black-Hole Binaries." 2006. p. 56.[11]

Section 4.2.1.

4.3 PDS and QPO Results of Phase Zones

4.3.1 All ρ Observations: Zone Overview

Figure 4-4 contains 12 PDS: one set of three energy windows for each of the four phase zones of the ρ cycle. The importance of phase zones is immediately evident–PDS of different zones appear significantly different. Significant QPOs are noted with arrows, and the fits of those features appear in Table 4.2. While detailed discussion of each phase zone including topics of sub-class results are organized in Sections 4.3.2-4.3.5, the general differences are clear. First, zones 2 and 3 (low X-ray count rate) contain the majority of LFQPO activity, while zones 1 and 4 clearly show weak LFQPO activity in the hard energy window. Zone 1 contains all 67 Hz activity–5.02σ in the medium-hard band (recall the entire ρ variability cycle 3.50σ medium-hard 67 Hz result). Finally, zones 3 and 4 (low soft color) have broad QPOs in the sum and medium-hard windows ranging from 150-160 Hz.

4.3.2 Zone 1: Flaring, High Soft Color

Figure 4-5 illustrates the location of zone 1 in color-intensity and color-color diagrams for each ρ sub-class. PDS for zone 1, broken down into each ρ sub-class and each energy window, are shown in Figure 4-6. Significant QPOs are marked with arrows, and the fitting results for these QPOs appear in Table 4.3 The PDS of all 82 ρ observations appears in Figure 4-4.

The immediately striking feature of Zone 1 is the appearence of the 67 Hz HFQPO in the sum and medium-hard bands. Zone 1 effectively isolates the 67 Hz HFQPO (Section 4.3.1), and suggests that this zone contains the excitation mechanism for that QPO. While HFQPOs are often (and always above 100 Hz) linked with the SPL state, the 67 Hz HFQPO has been known to appear in some of the thermal states of GRS 1915+105 (section 3.2.3). The appearance of a broad 48.59 Hz feature in the

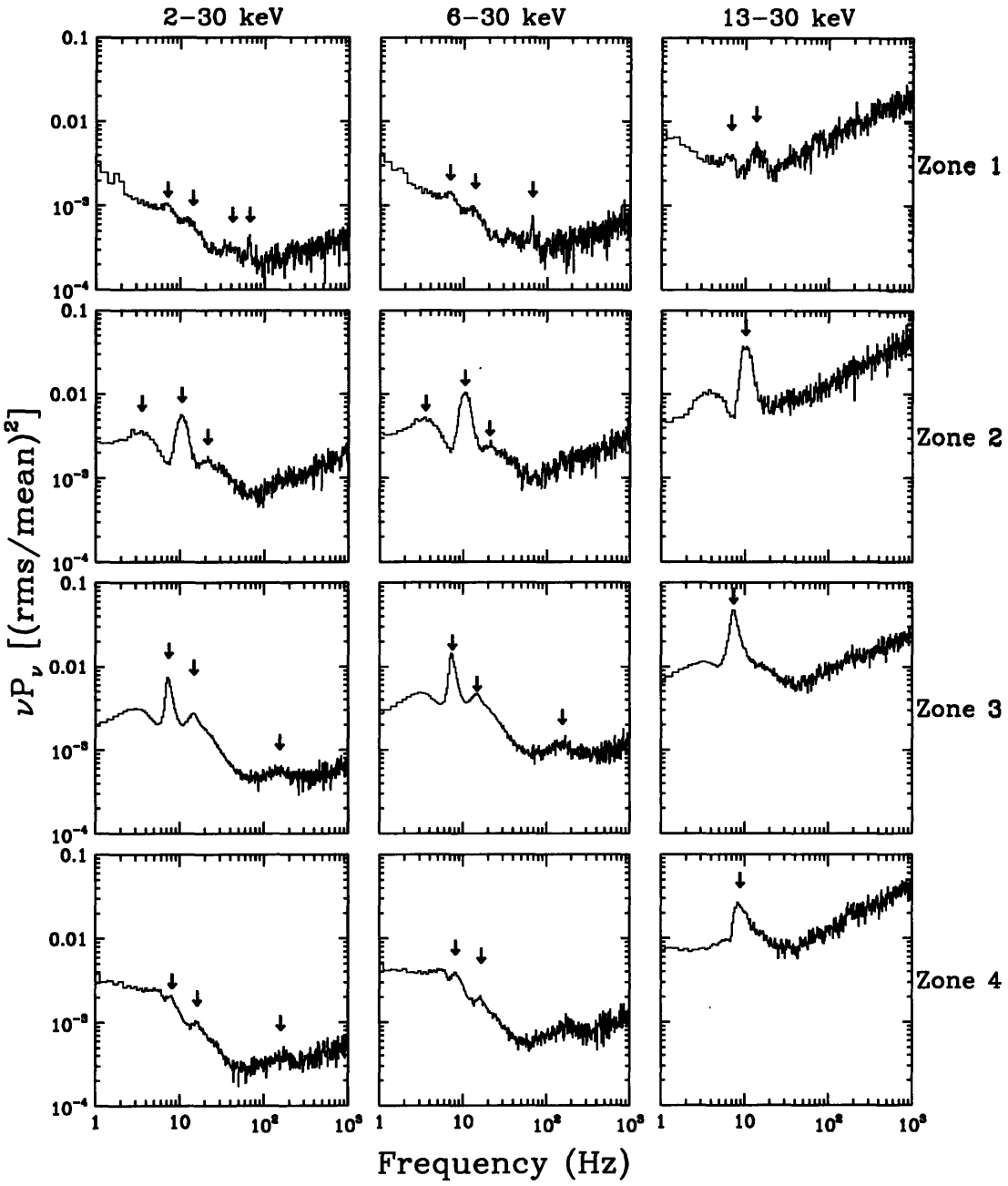

Figure 4-4: 12 PDS representing each zone and energy band of study. Each PDS represents data from all 82 ρ observations. Each column represents one energy window, as labeled atop the figure. Each row is one zone, as noted by labels on right of figure. Arrows mark significant ($>3\sigma$) detections. Fit parameters for marked results are tabulated in Table 4.2.

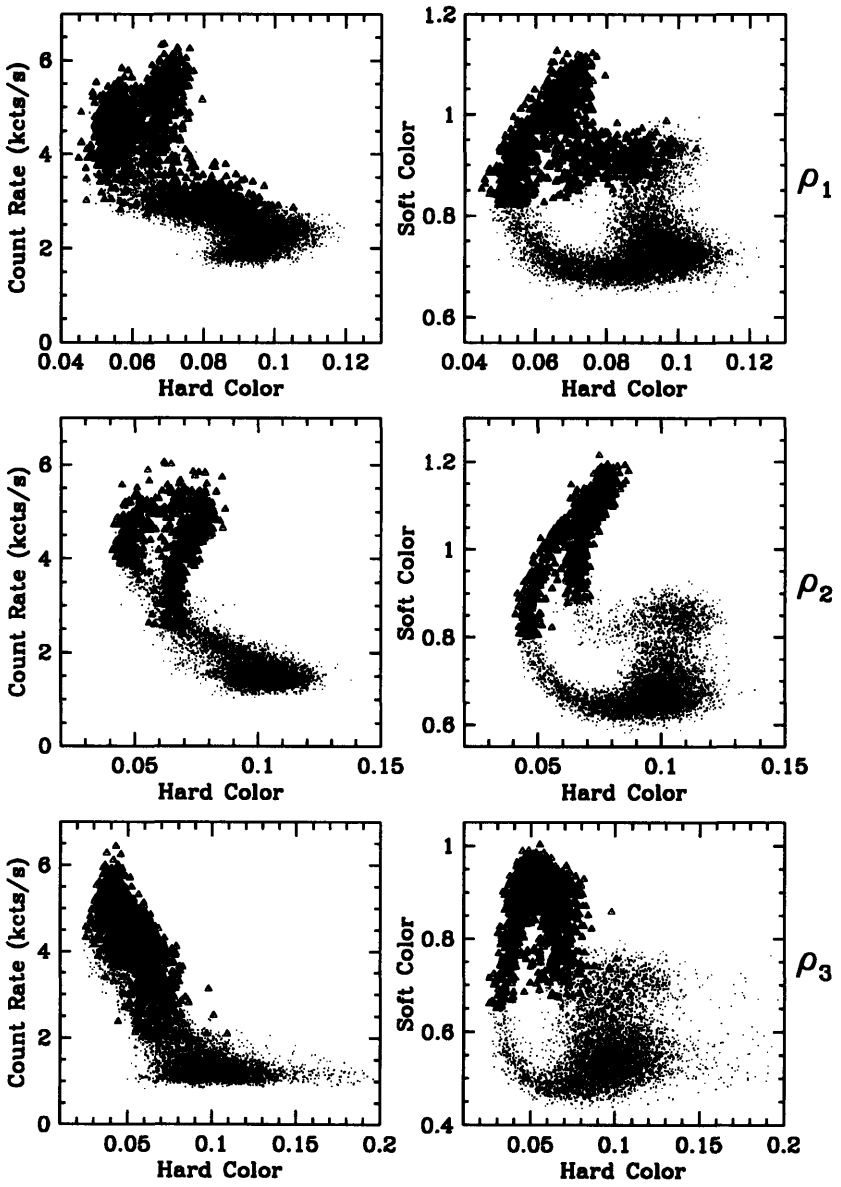

Figure 4-5: Illustration of zone 1 in color-intensity and color-color diagrams: ρ_1 (top), ρ_2 (middle), ρ_3 (bottom).

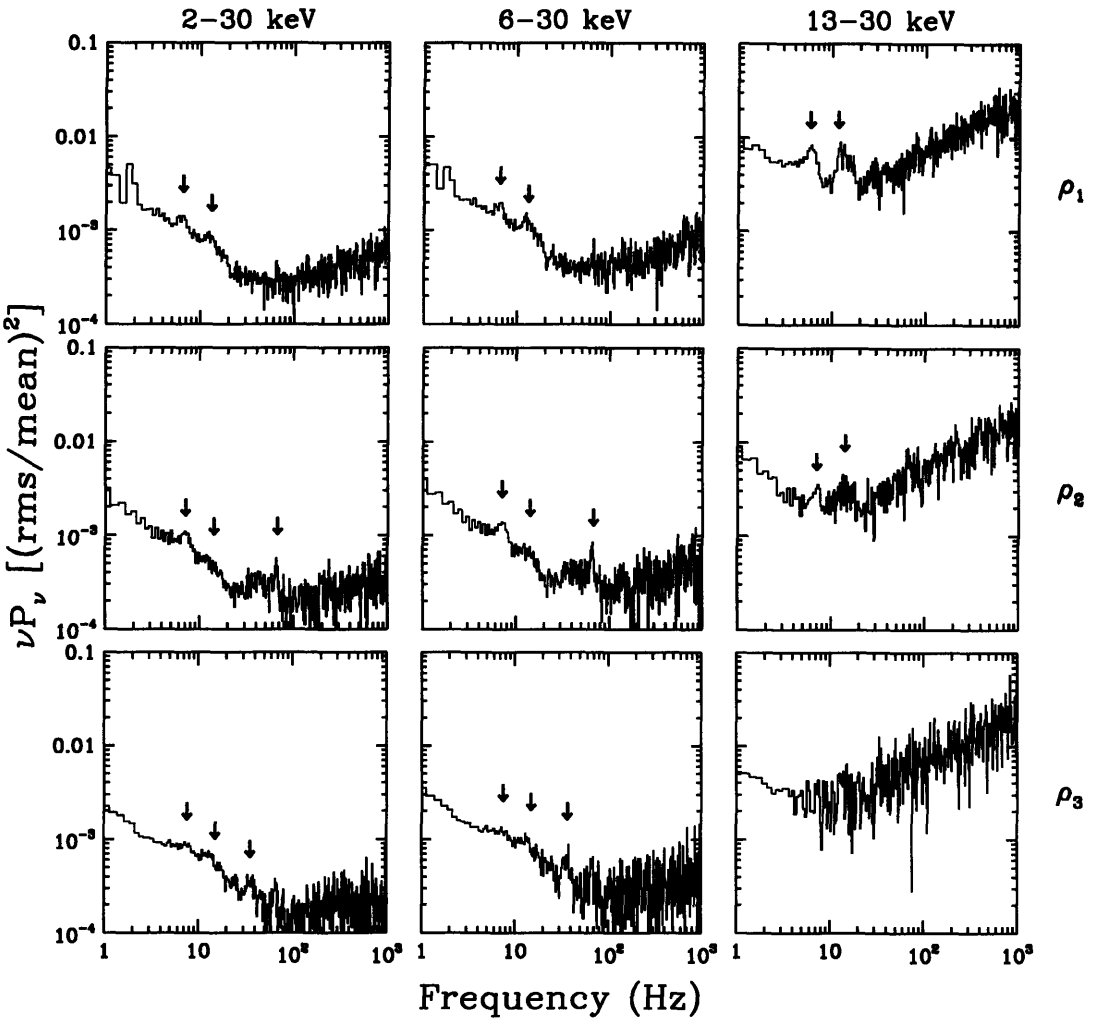

Figure 4-6: 9 PDS representing each energy window and each sub-class for zone 1 (flaring, high soft color) data. Arrows mark significant HFQPO results, tabulated in Table 4.3.

Zone	Energy Band	ν	χ^2	Q	rms	σ_{fit}
1 (ν_o)	2-30 keV	6.70	1.27	5.76	0.01553	5.32
1 ($2\nu_o$)	2-30 keV	13.41	—	5.26	0.02467	7.76
1	2-30 keV	41.45	0.89	3.58	0.00471	4.49
1	2-30 keV	65.95	0.56	30.39	0.00320	4.94
1 (ν_o)	6-30 keV	6.92	5.73^{p}	4.07	0.01278	23.42
1 ($2\nu_o$)	6-30 keV	13.84	—	4.87	0.00873	15.84
1	6-30 keV	66.13	0.42	28.02	0.00457	5.02
1	13-30 keV	13.47	2.07	20.14	0.02289	7.28
2	2-30 keV	3.56	$21.99^{p,c}$	2.13	0.03002	36.29
2 (ν_o)	2-30 keV	10.64	32.83^{c}	5.57	0.03438	78.36
2 ($2\nu_o$)	2-30 keV	21.28	—	15.88	0.00544	4.89
2	6-30 keV	3.55	$18.55^{p,c}$	2.13	0.03757	36.81
2 (ν_o)	6-30 keV	10.48	6.78^{c}	3.80	0.06221	117.94
2 ($2\nu_o$)	6-30 keV	21.24	—	6.99	0.01097	15.62
2	13-30 keV	10.36	8.38^{c}	4.37	0.10877	54.87
3 (ν_o)	2-30 keV	7.42	$129.33^{p,c}$	8.63	0.03190	183.94
3 ($2\nu_o$)	2-30 keV	14.83	—	4.06	0.01954	92.94
3	2-30 keV	153.59	0.73	4.93	0.00562	4.16
3 (ν_o)	6-30 keV	7.45	$94.79^{p,c}$	7.52	0.04849	194.38
3 ($2\nu_o$)	6-30 keV	14.90	—	3.89	0.02487	79.35
3	6-30 keV	150.61	0.62	3.18	0.01151	7.28
3	13-30 keV	7.42	10.94^{p}	4.82	0.11124	138.18
4 (ν_o)	6-30 keV	8.04	5.11^{c}	8.20	0.00956	23.36
4 ($2\nu_o$)	6-30 keV	16.07	—	7.44	0.00719	18.22
4	2-30 keV	157.55	0.39	2.74	0.00596	3.34
4 (ν_o)	6-30 keV	8.22	14.39^{c}	6.85	0.01480	24.75
4 ($2\nu_o$)	6-30 keV	16.45	—	14.82	0.00614	8.77
4	13-30 keV	8.85	3.96	2.87	0.09842	56.46

Table 4.2: Significant QPO results for the ρ phase zone study. All 82 ρ observations are included in these fits.

ρ_2 2-30 keV PDS has a coherence (Q = 1.92) too low to be legitimately considered a QPO.

LFQPOs at ~7 Hz (with harmonics at ~13 Hz) are far weaker than similar LFQPOs in zones 2 and 3, still suggest a nonthermal spectrum (rms amplitudes $\approx$.012). Power continuum levels between .11 and .13 ($r_{\rho_1} = 0.137$, $r_{\rho_2} = 0.139$, $r_{\rho_3} = 0.112$) again suggest nonthermal activity. Hard color values of zone 1 data are almost entirely less than the "hard" spectral border, suggesting thermal or SPL state. The combina-

tion of a soft spectrum, continuum power with $0.075 < r < 0.15$, and LFQPOs with rms > 1% clearly suggest that zone 1 is in the SPL state.

Sub-class	Energy Band	ν	χ^2	Q	rms	σ_{fit}
ρ_1 (ν_o)	2-30 keV	6.57	7.62[c]	5.34	0.01160	17.24
ρ_1 ($2\nu_o$)	2-30 keV	13.13	—	4.12	0.00984	15.65
ρ_1 (ν_o)	6-30 keV	6.58	3.99	6.78	0.01253	15.87
ρ_1 ($2\nu_o$)	6-30 keV	13.16	—	5.72	0.01359	15.92
ρ_1 (ν_o)	13-30 keV	5.87	1.29	6.52	0.03024	8.90
ρ_1 ($2\nu_o$)	13-30 keV	11.75	—	9.33	0.02449	5.59
ρ_2 (ν_o)	2-30 keV	7.05	4.58	3.98	0.01270	22.90
ρ_2 ($2\nu_o$)	2-30 keV	14.09	—	4.94	0.00442	6.98
ρ_2	2-30 keV	65.92	0.50	24.05	0.00453	5.32
ρ_2 (ν_o)	6-30 keV	7.06	3.73	4.74	0.01372	19.23
ρ_2 ($2\nu_o$)	6-30 keV	14.12	—	7.02	0.00588	6.38
ρ_2	6-30 keV	65.80	0.56	13.16	0.00785	5.92
ρ_2 (ν_o)	13-30 keV	7.11	0.92	8.89	0.01609	4.02
ρ_2 ($2\nu_o$)	13-30 keV	14.22	—	4.06	0.02365	4.63
ρ_3 (ν_o)	2-30 keV	7.53	2.81	3.94	0.00796	8.73
ρ_3 ($2\nu_o$)	2-30 keV	15.05	—	3.31	0.00561	6.54
ρ_3	2-30 keV	35.78	0.39	7.16	0.00470	3.65
ρ_3 (ν_o)	6-30 keV	7.36	1.99	3.35	0.00997	7.21
ρ_3 ($2\nu_o$)	6-30 keV	14.73	—	3.82	0.00766	6.59
ρ_3	6-30 keV	36.31	0.42	7.26	0.00652	3.83

Table 4.3: QPO fitting results for significant zone 1 (flaring, high soft color) results.

Differences between ρ sub-classes in Zone 1 are clear in the detections of 67 Hz. The PDS ρ_2 observations contains strong detections of 5.32σ at 65.92 Hz in the sum band and 5.62σ at 65.94 Hz in the medium-hard band. These results are far stronger than in the average of all ρ sub-classes and zones (3.50σ), and even exceed the detection in all 82 ρ observations in zone 1 (5.09σ). This is a significant result considering that the ρ_2 group contains only 31% of the entire ρ exposure time. Weak features at 67 Hz are seen in the sum and medium-hard PDS for both ρ_1 and ρ_2 groups, but the detections are too weak ($<3\sigma$) for note. In the case of ρ_3, the lack of a significant detection is not sufficient to exclude the average presence of a 67 Hz oscillation since ρ_3 represents only 15% of the total ρ exposure.

4.3.3 Zone 2: Low Count Rate and High Soft Color

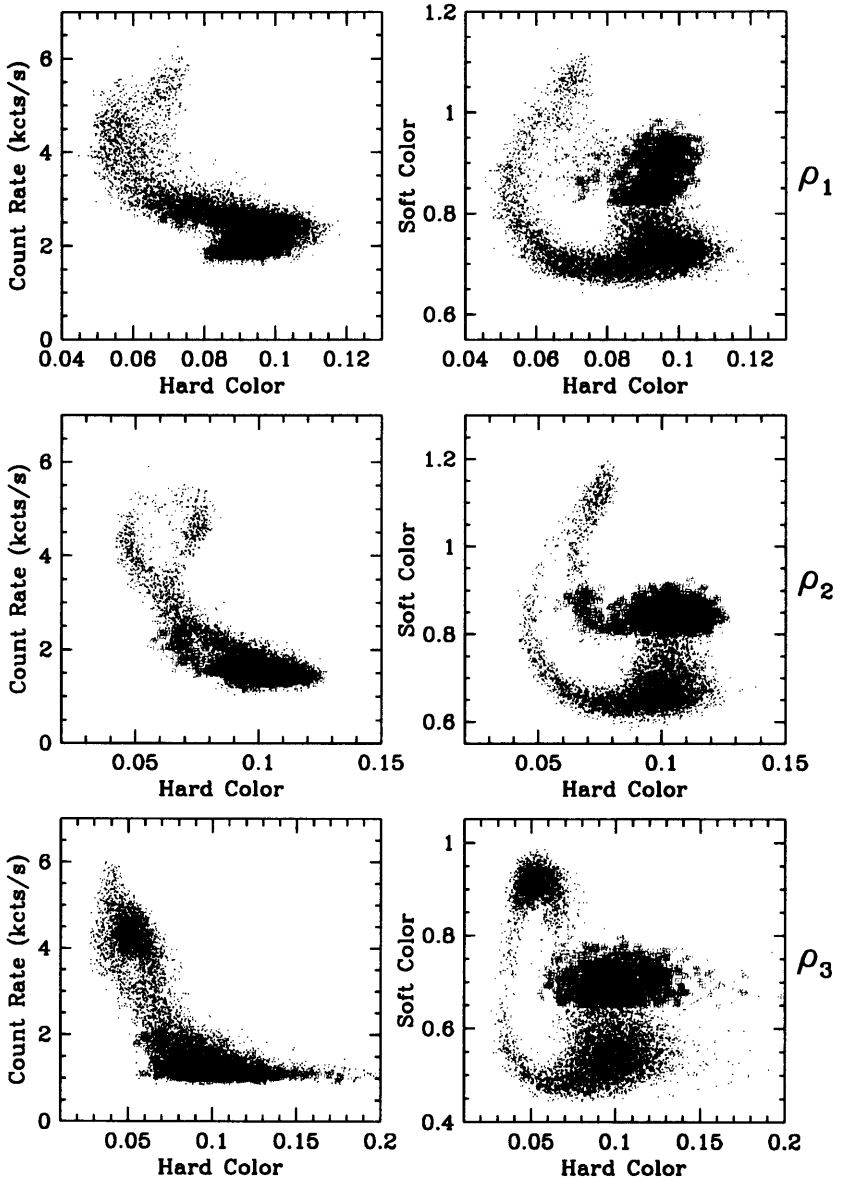

Figure 4-7: Illustration of zone 2 in color-intensity and color-color diagrams: ρ_1 (top), ρ_2 (middle), ρ_3 (bottom).

Figure 4-7 illustrates the location of zone 2 in color-intensity and color-color diagrams for each ρ sub-class. PDS for each ρ sub-class in each energy window are shown in Figure 4-8. Significant QPOs are marked with arrows, and the fitting results for

these QPOs appear in Table 4.4 The PDS of all 82 ρ Zone 2 observations appears in Figure 4-4. Figure 4-8 clarifies the location of zone 2 in color-intensity and color-color diagrams.

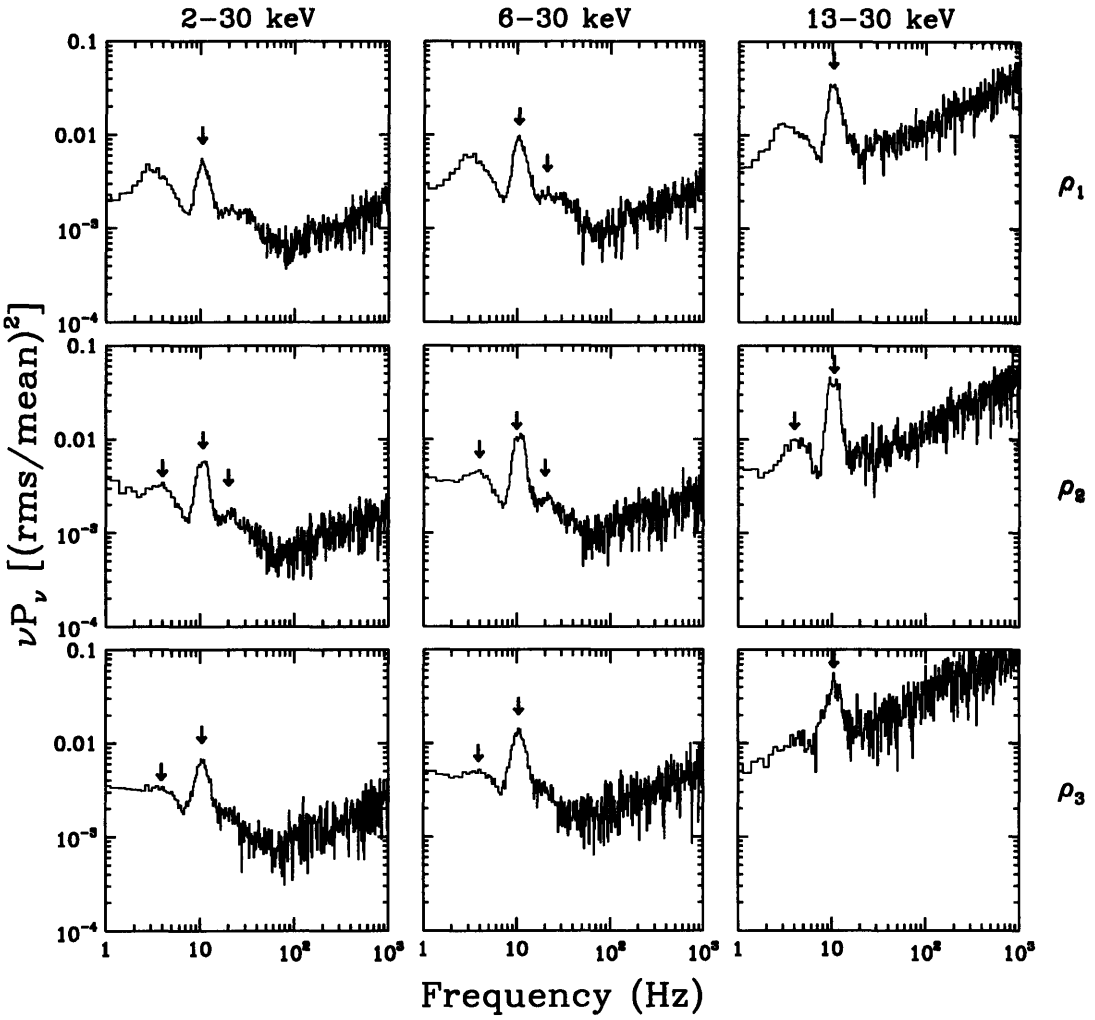

Figure 4-8: 9 PDS representing each energy window and each sub-class for zone 2 (quiet, high soft color) data. Arrows mark significant HFQPO results, tabulated in Table 4.4.

Zone 2 PDS show no significant ($>3\sigma$) HFQPO detections, though ρ_1 sum and medium-hard bands do show well fit ($\chi^2 < .5$) $\sim 2.5\sigma$ detections at 151 Hz.

The LFQPOs of Zone 2 are strong and non-sinusoidal (evident in harmonics) in each sub-class and all but the 13-30 energy window, where no harmonics are detected.

Sub-class	Energy Band	ν	χ^2	Q	rms	σ_{fit}
ρ_1	2-30 keV	10.43	4.55	4.78	0.03553	55.76
ρ_1 (ν_o)	6-30 keV	10.56	$29.13^{p,c}$	5.56	0.04587	56.94
ρ_1 ($2\nu_o$)	6-30 keV	21.12	—	4.80	0.01133	6.55
ρ_1	13-30 keV	10.31	4.49	4.62	0.10054	36.49
ρ_2	2-30 keV	4.01	13.10^{p}	3.13	0.02135	16.53
ρ_2 (ν_o)	2-30 keV	10.80	$8.50^{p,c}$	4.89	0.04011	61.88
ρ_2 ($2\nu_o$)	2-30 keV	21.60	—	5.17	0.01300	12.97
ρ_2	6-30 keV	3.99	$5.54^{p,c}$	2.75	0.02940	18.14
ρ_2 (ν_o)	6-30 keV	10.79	$13.54^{p,c}$	4.80	0.05711	67.85
ρ_2 ($2\nu_o$)	6-30 keV	21.59	—	6.06	0.01483	11.38
ρ_2	13-30 keV	3.99	1.72	2.28	0.06008	12.35
ρ_2	13-30 keV	10.46	4.68	4.10	0.12248	41.78
ρ_3	2-30 keV	3.91	4.04	3.59	0.01527	7.13
ρ_3	2-30 keV	10.53	3.97	4.15	0.04387	46.50
ρ_3	6-30 keV	3.93	1.93	2.91	0.02454	9.34
ρ_3	6-30 keV	10.48	3.86	4.05	0.06590	49.91
ρ_3	13-30 keV	10.51	0.72	3.38	0.12481	15.35

Table 4.4: QPO fitting results for significant zone 2 (quiet, high soft color) results.

The ~10Hz QPO (15σ-70σ depending on energy window) requires a nonthermal state classification in zone 2, while power continuum levels ($r_{\rho_1} = 0.114$, $r_{\rho_2} = 0.108$, $r_{\rho_3} = 0.122$) also rule out the thermal state. LFQPOs are seen most often in the SPL and H:SPL intermediate state, and the high hard color values of zone 2 data suggests a spectral state harder than SPL. The combination of a hard spectrum, continuum power $r > .1$, and LFQPOs with rms > 1% indicate that zone 2 is in a hard or H:SPL intermediate spectral state.

QPO fitting results and power continuum levels do not show significant differences between sub-classes in phase zone 2. The strength of the QPO at ~4 Hz appears to decrease from ρ_1 to ρ_2 and nearly disappears in ρ_3, and may shift in frequency as well. The similarity between sub-classes in zone 2 suggests that this zone does not show differences between the sub-classes.

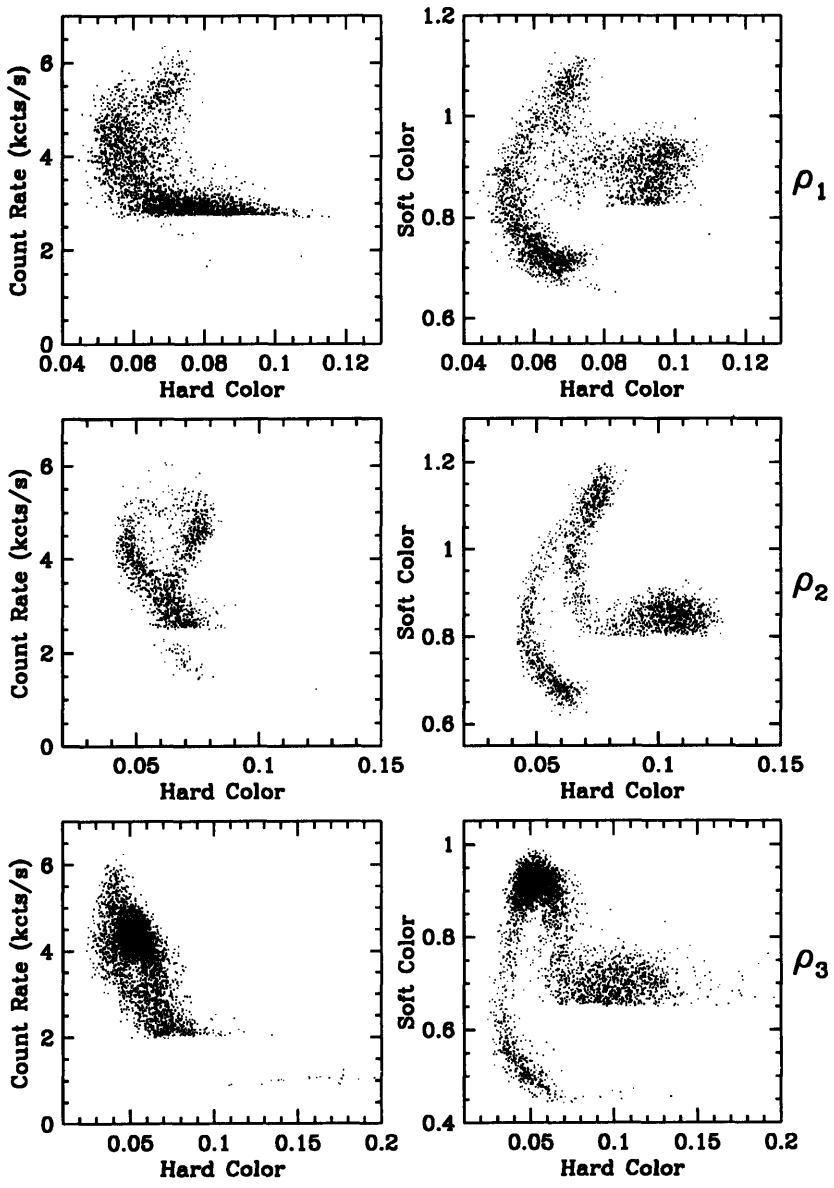

Figure 4-9: Illustration of zone 3 in color-intensity and color-color diagrams: ρ_1 (top), ρ_2 (middle), ρ_3 (bottom).

4.3.4 Zone 3: Low Count Rate and Low Soft Color

Figure 4-9 illustrates the location of zone 3 in color-intensity and color-color diagrams for each ρ sub-class. PDS for zone 3 in each ρ sub-class and energy band are shown in Figure 4-10. Significant QPOs are marked with arrows, and the fitting results for these QPOs appear in Table 4.5 The PDS of all 82 ρ zone 3 observations appears in Figure 4-4.

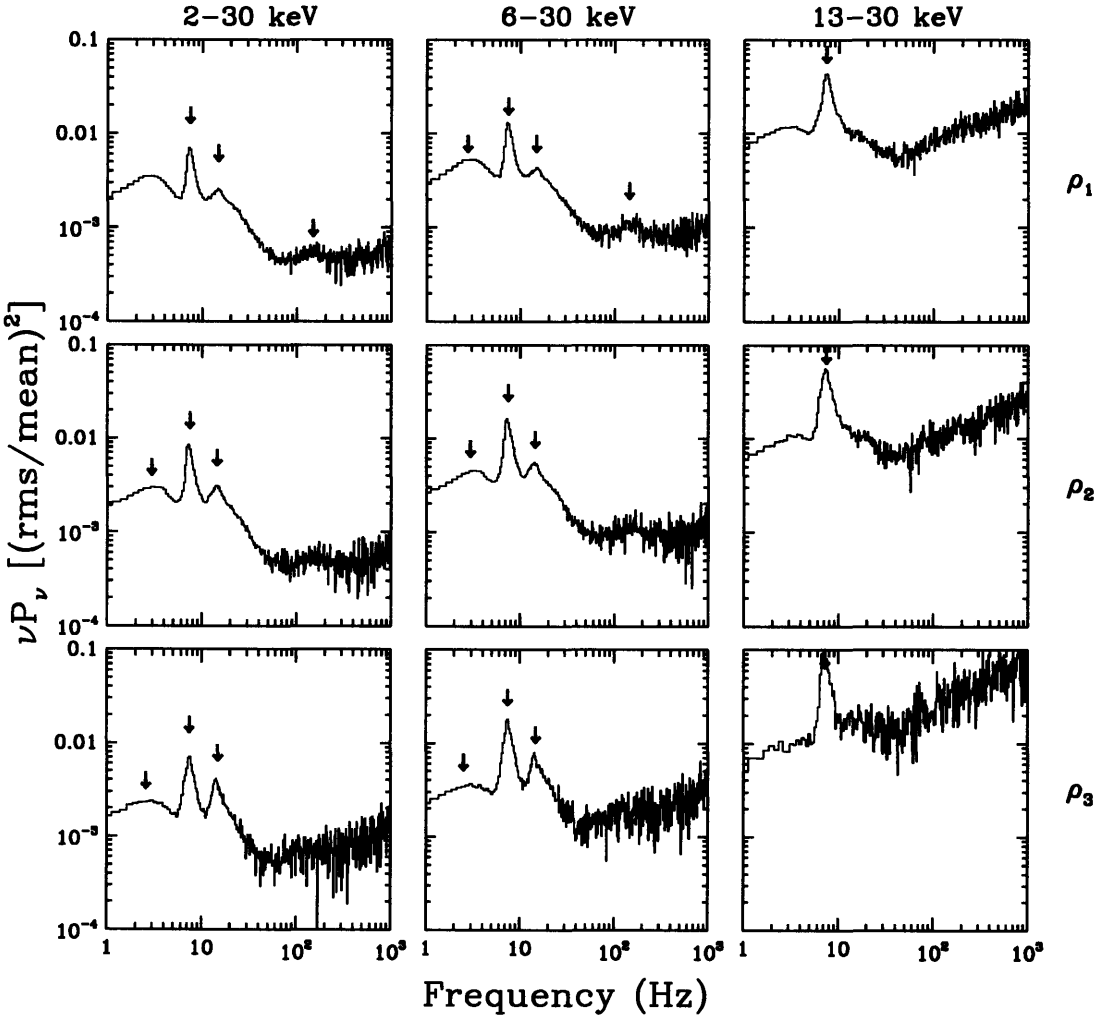

Figure 4-10: 9 PDS representing each energy window and each sub-class for zone 3 (quiet, low soft color) data. Arrows mark significant HFQPO results, tabulated in Table 4.5.

The zone 3 ~150 Hz HFQPO echoes the feature in the PDS for all 82 zone 3

observations (detected at 7.28 σ in the 6-30 keV band at 150 $\pm$ 6.53 Hz). This QPO is clearly detected for the ρ_1 group and weakly detected in the ρ_2 group in the 2-30 keV (sum) band (see Table 4.5). This HFQPO is broad, but coherence values (sum: $Q_{\rho_{all}} = 3.17 \pm .55$, $Q_{\rho_1} = 3.36 \pm .73$, $Q_{\rho_2} = 5.06 \pm 2.37$) clearly indicate a QPO rather than a broad power peak.

Sub-class	Energy Band	ν	χ^2	Q	rms	σ_{fit}
ρ_1 (ν_o)	2-30 keV	7.39	23.50[c]	7.63	0.03343	140.23
ρ_1 ($2\nu_o$)	2-30 keV	14.79	—	7.14	0.01129	36.04
ρ_1	2-30 keV	148.00	0.53	4.43	0.00663	4.58
ρ_1	6-30 keV	2.74	74.65[p,c]	2.06	0.03467	66.30
ρ_1 (ν_o)	6-30 keV	7.41	19.00[c]	7.06	0.04823	144.00
ρ_1 ($2\nu_o$)	6-30 keV	14.82	—	7.45	0.01248	26.11
ρ_1	6-30 keV	146.01	0.53	3.36	0.01130	5.69
ρ_1	13-30 keV	7.46	5.32[c]	5.04	0.10299	98.89
ρ_2	2-30 keV	2.92	54.05[p,c]	2.41	0.02191	43.13
ρ_2 (ν_o)	2-30 keV	7.30	20.29[c]	7.37	0.03792	122.45
ρ_2 ($2\nu_o$)	2-30 keV	14.61	—	6.73	0.01511	43.13
ρ_2	6-30 keV	2.96	36.11[p,c]	2.62	0.02445	35.84
ρ_2 (ν_o)	6-30 keV	7.34	19.76[c]	6.99	0.05481	124.42
ρ_2 ($2\nu_o$)	6-30 keV	14.80	—	7.72	0.01678	31.25
ρ_2	13-30 keV	7.33	6.81[p]	4.36	0.12854	96.16
ρ_3	2-30 keV	2.58	17.67[p]	2.43	0.01612	15.49
ρ_3 (ν_o)	2-30 keV	7.45	12.80[c]	7.09	0.03457	61.11
ρ_3 ($2\nu_o$)	2-30 keV	14.89	—	4.55	0.02702	46.04
ρ_3	6-30 keV	2.50	6.28[p]	2.19	0.02197	10.47
ρ_3 (ν_o)	6-30 keV	7.48	9.76[c]	6.45	0.06053	71.08
ρ_3 ($2\nu_o$)	6-30 keV	14.96	—	4.53	0.03415	33.33
ρ_3	13-30 keV	7.20	2.55	5.76	0.15201	40.72

Table 4.5: QPO fitting results for significant zone 3 (low count rate, low soft color) results.

Zone 3 shares the trait of strong LFQPOs with zone 2, but differs in important ways. First, the strongest zone 3 LFQPO is narrower than that of zone 2, and is centered at ~7.5 Hz as opposed to ~10 Hz. While LFQPOs have been found to vary in frequency within minutes,[3] this change occurs within seconds, i.e. the timescale in which GRS 1915+105 switches from zone 2 to zone 3 in each individual ρ cycle.

[3]Remillard, R.A. and McClintock, J.E. "X-Ray Properties of Black-Hole Binaries." 2006. p. 77.[11].

The $.5\nu_o$ and $2\nu_o$ harmonics of the ~7.5 Hz result, which suggests the fundamental oscillation deviates from a sinusoidal profile, are fit with a large χ^2. This poor value of χ^2 is due to the non-Lorentzian profile of the ~3.7 Hz QPOs and the difficulty in establishing a suitable continuum level due to the width of that LFQPO.

LFQPOs mark a nonthermal accretion system. The power continuum values for zone 3 (r_{ρ_1} = 0.099, r_{ρ_2} = 0.099, r_{ρ_3} = 0.093) are just below the r >.1 requirement for hard state. The hard color of zone 3 suggests a hard spectrum which, combined with the LFQPOs and power continuum values, suggest that zone 3 is in a H:SPL intermediate state.

LFQPO differences between sub-classes in zone 3 are limited to the apparent strengthening of the ~15 Hz QPO harmonic in ρ_3.

4.3.5 Zone 4: Flaring, Low Soft Color

Figure 4-11 illustrates the location of zone 4 in color-intensity and color-color diagrams for each ρ sub-class. PDS for zone 4 in each ρ sub-class and energy band are shown in Figure 4-12. Significant QPOs are marked with arrows, and the fitting results for these QPOs appear in Table 4.6 The PDS of all 82 ρ zone 4 observations appears in Figure 4-4.

Phase zone 4 shows a hint of a broad feature in the 6-30 keV band for the ρ_2 group, but none of the fits yields a 3σ HFQPO detection.

Zone 4 ~8 Hz LFQPOs with $2\nu_o$ harmonics and rms > 1% suggest a nonthermal state. The color-color diagram of zone 4 crosses the hard color state discrimination lines suggesting a mixture of the SPL and harder states. Power continuum levels (r_{ρ_1} = 0.121, r_{ρ_2} = 0.131, r_{ρ_3} = 0.131) again reinforce a nonthermal result but do not clearly distinguish between a SPL or H:SPL intermediate state. We conclude that zone 4 combines the SPL and either the hard or H:SPL intermediate state.

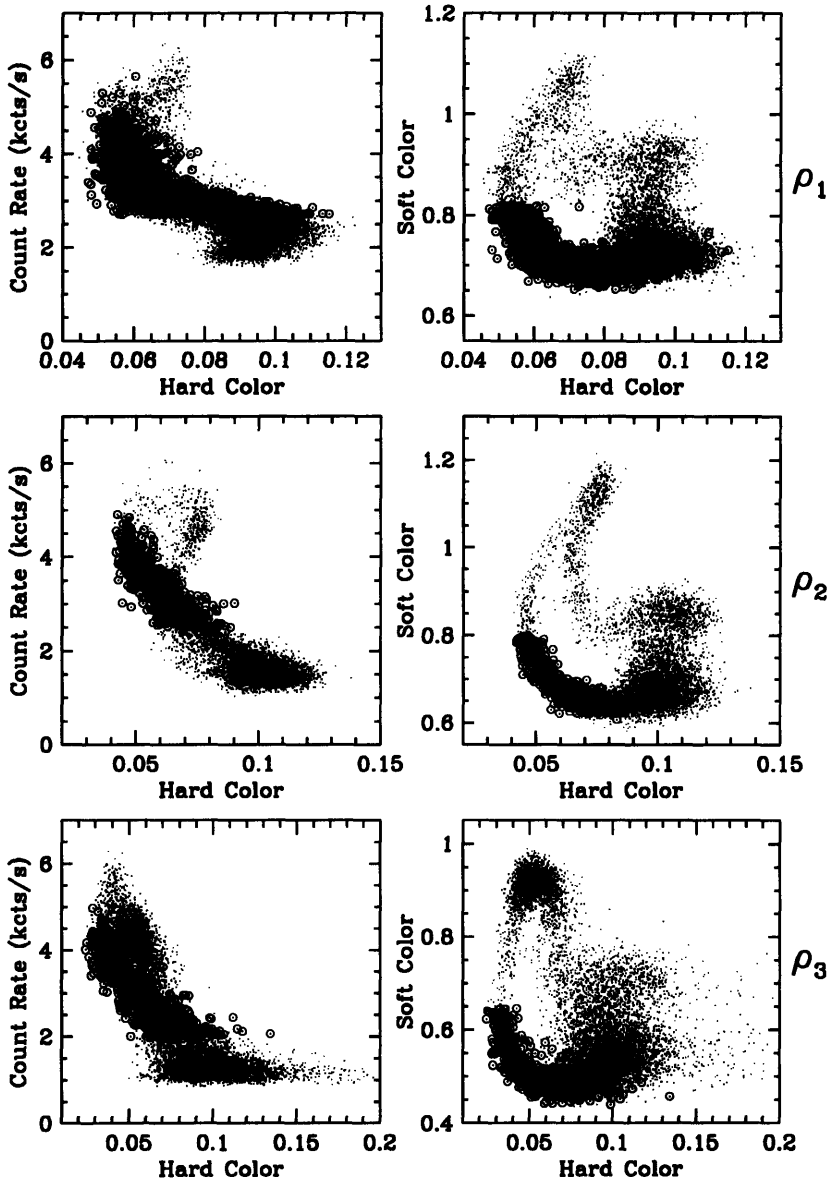

Figure 4-11: Illustration of zone 4 in color-intensity and color-color diagrams: ρ_1 (top), ρ_2 (middle), ρ_3 (bottom).

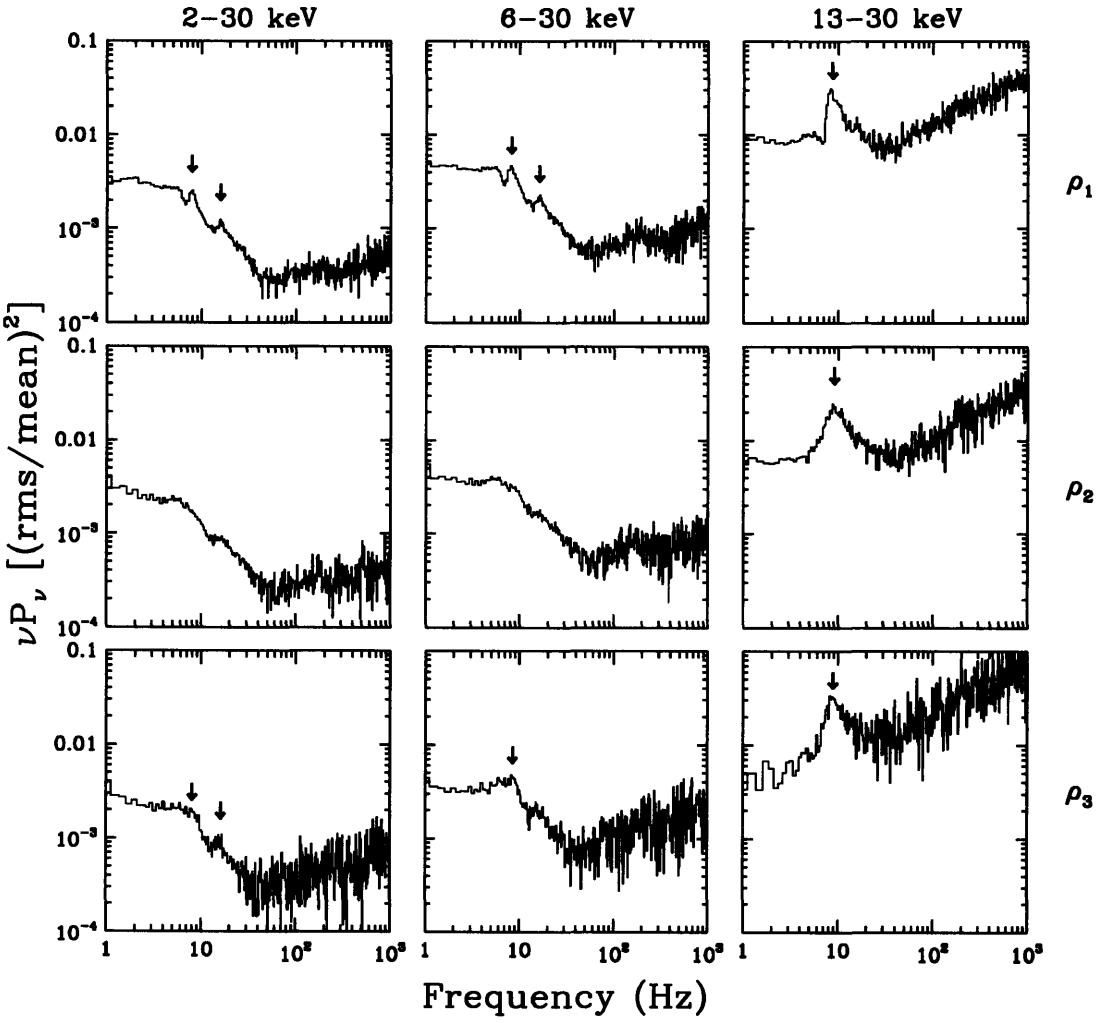

Figure 4-12: 9 PDS representing each energy window and each sub-class for zone 4 (flaring, low soft color) data. Arrows mark significant HFQPO results, tabulated in Table 4.6.

Sub-class	Energy Band	ν	χ^2	Q	rms	σ_{fit}
ρ_1 (ν_o)	2-30 keV	7.95	12.82[c]	11.69	0.01094	25.34
ρ_1 ($2\nu_o$)	2-30 keV	15.90	—	11.44	0.00619	12.52
ρ_1 (ν_o)	6-30 keV	8.12	10.76[c]	9.78	0.01630	25.75
ρ_1 ($2\nu_o$)	6-30 keV	16.25	—	12.22	0.00816	10.42
ρ_1	13-30 keV	8.65	4.72	3.66	0.09255	41.85
ρ_2	13-30 keV	9.08	1.20	2.16	0.10758	37.67
ρ_3 (ν_o)	2-30 keV	8.01	3.21	6.46	0.01096	9.24
ρ_3 ($2\nu_o$)	2-30 keV	16.02	—	10.90	0.00504	3.39
ρ_3	6-30 keV	8.42	2.79	5.69	0.02147	13.02
ρ_3	13-30 keV	8.93	0.63	2.76	0.11598	14.49

Table 4.6: HFQPO fitting results for significant zone 4 (flaring, low soft color) results.

4.3.6 Overview of Zone Results

We isolate the 67 Hz QPO in the ρ cycle to zone 1, a high count rate and high soft color zone likely of SPL state. The GRS 1915+105 QPO at 67 Hz is further isolated to the ρ_2 and ρ_3 sub-classes. Recalling the γ-box (Figure 3-8), we conclude that the 67 Hz QPO in the ρ cycle is excited while the source occupies a similar region in the X-ray color-color diagram. The broad HFQPO at ~145 Hz is isolated to zone 3 of ρ_1 observations. Zone 3 indicates a hard or H:SPL intermediate state. While all sub-classes show LFQPOs in all zones, the LFQPO detections in zones 2 and 3 are stronger except in the 13-30 keV (hard) band where all zones show similar detections. Furthermore, we find that LFQPO detections center at ~8 Hz in zones 1, 3, and 4 but center at ~10 Hz in zone 2. These QPOs would not survive the data selections over thousands of ρ cycles if they moved in frequency by a significant amount. These differences in QPO detections, both in low and high frequency domains, highlight the speed with which GRS 1915+105 moves between different modes of radiation. In a similarly interesting note, the excitation of a strong LFQPO in the hard window of every phase zone and the location of a broad HFQPO hear 150 Hz fine tune these oscillations to specific phases of the ρ cycle.

We find the zones of study, as defined by soft color and count rate, do change in spectral state. Results suggest that zone 1 is in a SPL state, zones 2 and 3 in H:SPL

intermediate state, and that zone 4 marks a return to the SPL state with some mixing with a harder state (i.e. hard or H:SPL intermediate). Without spectral modeling these state results cannot be verified. The relatively weaker detection of LFQPOs in the softer hard color zones 1 and 4 suggest that a method of zoning the ρ phase based exclusively on segments of the color-color diagram might isolate a region of the ρ cycle in a thermal state.

Chapter 5

Summary and Conclusions

5.1 The Properties of the ρ Cycle

Properties of ρ-type instability cycles in X-ray color and intensity of the black hole binary GRS 1915+105 were investigated for mean recurrence time (τ) and shape of the rapid double flares that characterize this behavior.

- 33.73 s $\leq \tau \leq$ 122.49 s; $<\tau> \pm \sigma_{sample} = 65.44 \pm 19.83$ s
- Flare fraction (ζ defined as fraction $\geq$ 1.2*mean count rate) ranges 12.11% $\leq \zeta \leq$ 37.61%; $<\zeta> \pm \sigma_{sample} = 20.05 \pm 5.33\%$.
- 3 ρ sub-classes defined using τ and ζ.
  - ρ_1 are slow cycles. ρ_2 and ρ_3 have similar τ (~45 s) but $\zeta_{\rho_3} > \zeta_{\rho_2}$.
  - Physical differences between ρ sub-classes are reinforced by unequal excitation of the 67 Hz QPO. Strongest detection found in ρ_3: 4.14σ at 66.86 $\pm$ 0.86 Hz, coherence Q = 33.95. No detection in ρ_1.
- Flare amplitudes (relative to minimum flux in the cycle) are not correlated with ρ sub-class and the distribution shows a maximum cutoff value near 3500 cts/s/PCU (i.e. flux equivalent of 1.4 Crab).

- Flare maxima in ρ cycle are consistent with the Eddington limit–we suggest this Eddington limit as one of the causes of ρ sub-class evolution in the τ, ζ plane. The reason for the τ minimum remains unknown.

5.2 Phase Zones within the ρ Cycle

ρ-type cycles of the black hole binary GRS 1915+105 were separated into four phase intervals to isolate flaring and color changes. PDS for each zone (and ρ sub-class) were then computed to investigate QPO properties and power continuum strength. Spectral and timing results were combined to estimate the black hole binary spectral state for each zone. While the results indicate no zone of thermal state, a different method of zoning the variability cycle may provide different results.

- Divisions were made in count rate (X) and soft X-ray color (S; 5-12/2-5 keV.)
  - Zone 1: high X and high S.. zone 2: low X and high S, zone 3: low X and low S, zone 4: high X and low S. Boundaries: $X_{\rho_1} = 2700$, $S_{\rho_1} = 0.82$, $X_{\rho_2} = 2500$, $S_{\rho_1} = 0.80$, $X_{\rho_3} = 2000$, $S_{\rho_1} = 0.65$,
- We localized 67 Hz to zone 1: the second of doubly-peaked ρ flares, with harder color than the first peak, and results indicate a steep power law state in zone 1, and further to zone 1 ρ_2 6-30 keV band with a 5.92σ detection at 65.8 ± 0.6 Hz, Q = 13.16.
- A ~150 Hz QPO was localized to zone 3, where results suggest a hard/steep power law intermediate state. (6-30 keV band detection of 5.69σ at 146.01 ± 7.30 Hz, Q = 3.36)
- Zones 2 and 3 contain the strongest LFQPO detections (~10.5 Hz and ~7.5 Hz, respectively).
- Results suggest that the ρ oscillation is SPL in zone 1 and 4, and hard or H:SPL intermediate state in zones 2 and 3.

– Flaring zones indicate SPL, quieter zones indicate H:SPL intermediate

The localization of the 67 Hz QPO to phase zone 1 of the ρ cycle, which occupies an X-ray color-color region similar to γ observations, confirms the correlation between 67 Hz activity and the location of the source in the X-ray color-color diagram. The γ-box (Figure 3-7) is therefore a useful tool to locate 67 Hz QPO activity in other GRS 1915+105 variable observation classes. This result further implies that the 67 Hz QPO is associated with a distinct spectral shape that we identify as within the SPL state. The flares of ρ-type observations are doubly-peaked, with the first soft in hard color, and the second hard. The soft peak we isolate to zone 4, and the hard peak to zone 1, and find that the 67 Hz QPO is detected in the hard, second peak of ρ-type flares. We localize the 150 Hz QPO in the averaged ρ PDS to zone 3, sub-class ρ_3. Thus the two HFQPOs of the ρ cycle are isolated to different phase zones, and also to different sub-classes. These results support previous work suggesting that HFQPOs may be isolated to phase intervals of variable observation cycles.[1]

We suggest spectral states for each phase zone: SPL in zones 1 and 4, hard or H:SPL intermediate states in zones 2 and 3. The power law component of the SPL state competes with a sizable thermal component, so a disk-based mechanism for the QPO at 67 Hz is likely.

5.3 Future Work

The tools developed for phase zoning, and producing PDS of phase zones may be immediately applied to other variable observations of GRS 1915+105 and any other X-ray novae observed by the RXTE program. More complete results compiled on all variable observation types may offer further verification for the importance of GRS 1915+105's location in a color-color diagram to the study of HFQPO excitation; especially for the 67 Hz and 150 Hz HFQPO pair. Variable observation types which exhibit no HFQPO activity in the overall mean PDS may be studied with this method

[1]Remillard, R. and Muno, M. and McClintock, J. E. and Orosz, J. "X-ray QPOs in black-hole binary systems." 2002.[9]

to determine if detections are possible in a particular phase zone. In addition, variable types with LFQPO detections, including ρ zones 1 and 4, can be phase searched for intervals in the thermal state.

This study examined spectral properties on a color-color diagram. Data is available to extend this analysis to coarse (16 bin) spectra of one second integration times. This would allow us to complete basic spectral fits within each phase zone. This will provide a better understanding of how the thermal and non-thermal spectral components compete in each phase zone and how quickly (down to one second resolution). The number of phase zones could be substantially increased for such an investigation. Possible spectral links to QPO excitation may be discovered, i.e. does QPO excitation match or lag behind any spectral change?

The topic of ρ sub-classes with significant disparities in two HFQPO excitations (67 Hz and 150 Hz) offers another method of studying spectral and timing effects on HFQPO production. What causes the correlation between zone and sub-class vs. HFQPO power? Rigorous spectral studies of the sub-classes and zones, and through defining more zones via phase-binning may provide insight to this question. As the differences between ρ sub-classes are limited (and easy to overlook), the possible physical mechanisms causing the 67 Hz QPO in ρ_2 zone 1 and the 150 Hz QPO in ρ_1 zone 3 can be investigated with continued research. Either HFQPO of the ρ cycle warrants further attention, but paired and phase separated, the 67 Hz and 150 Hz results provide special opportunities for continued investigation of the ρ-type cycle of GRS 1915+105.

Bibliography

[1] T. Belloni, M. Klein-Wolt, M. Méndez, M. van der Klis, and J. van Paradijs. A model-independent analysis of the variability of GRS 1915+105. *Astronomy and Astrophysics*, 355:271–290, March 2000.

[2] R. D. Blandford. *Lighthouses of the Universe: The Most Luminous Celestial Objects and Their Use for Cosmology.* Springer, 1 edition, 2002.

[3] H. et al. Bradt. *X-ray Timing Explorer: Taking the Pulse of the Universe.*

[4] J. Greiner, J. G. Cuby, and M. J. McCaughrean. An unusually massive stellar black hole in the Galaxy. *Nature*, 414:522–525, November 2001.

[5] J. Greiner, E. H. Morgan, and R. A. Remillard. Rossi X-Ray Timing Explorer Observations of GRS 1915+105. *The Astrophysical Journal*, 473:L107+, December 1996.

[6] J. Greiner, E. H. Morgan, and R. A. Remillard. RXTE spectroscopy of GRS 1915/+105. *New Astronomy Review*, 42:597–600, December 1998.

[7] E. H. Morgan, R. A. Remillard, and J. Greiner. RXTE Observations of QPOs in the Black Hole Candidate GRS 1915+105. *The Astrophysical Journal*, 482:993–+, June 1997.

[8] R. Remillard, M. Muno, J. E. McClintock, and J. Orosz. X-ray QPOs in black-hole binary systems. In *New Views on Microquasars*, pages 49–+, 2002.

[9] R. Remillard, M. Muno, J. E. McClintock, and J. Orosz. X-ray QPOs in black-hole binary systems. In P. Durouchoux, Y. Fuchs, and J. Rodriguez, editors, *New Views on Microquasars*, pages 49–+, 2002.

[10] R. A. Remillard. X-ray spectral states and high-frequency QPOs in black hole binaries. *Astronomische Nachrichten*, 326:804–807, November 2005.

[11] R. A. Remillard and J. E. McClintock. X-ray properties of black-hole binaries. In *Annu. Rev. Astron. Astrophys.*, pages 44:49–92. 10.1146/annurev.astro.44.051905.092532, 2006.

[12] Ronald A. Remillard and Jeffrey E. McClintock. *Compact Stellar X-ray Sources*, chapter 4, pages 1–58. Cambridge University Press, 2003.

[13] Kip S. Thorne. *Black Holes and Time Warps: Einstein's Outrageous Legacy*. W. W. Norton and Company, Inc., 1994.